A high-order discontinuous Galerkin method for wave propagation through coupled elastic–acoustic media

Lucas C. Wilcox [a,*], Georg Stadler [a], Carsten Burstedde [a], Omar Ghattas [a,b,c]

[a] Institute for Computational Engineering and Sciences, The University of Texas at Austin, Austin, TX 78712, USA
[b] Jackson School of Geosciences, The University of Texas at Austin, Austin, TX 78712, USA
[c] Department of Mechanical Engineering, The University of Texas at Austin, Austin, TX 78712, USA

ARTICLE INFO

ABSTRACT

We introduce a high-order discontinuous Galerkin (dG) scheme for the numerical solution of three-dimensional (3D) wave propagation problems in coupled elastic–acoustic media. A velocity–strain formulation is used, which allows for the solution of the acoustic and elastic wave equations within the same unified framework. Careful attention is directed at the derivation of a numerical flux that preserves high-order accuracy in the presence of material discontinuities, including elastic–acoustic interfaces. Explicit expressions for the 3D upwind numerical flux, derived as an exact solution for the relevant Riemann problem, are provided. The method supports *h*-non-conforming meshes, which are particularly effective at allowing local adaptation of the mesh size to resolve strong contrasts in the local wavelength, as well as dynamic adaptivity to track solution features. The use of high-order elements controls numerical dispersion, enabling propagation over many wave periods. We prove consistency and stability of the proposed dG scheme. To study the numerical accuracy and convergence of the proposed method, we compare against analytical solutions for wave propagation problems with interfaces, including Rayleigh, Lamb, Scholte, and Stoneley waves as well as plane waves impinging on an elastic–acoustic interface. Spectral rates of convergence are demonstrated for these problems, which include a non-conforming mesh case. Finally, we present scalability results for a parallel implementation of the proposed high-order dG scheme for large-scale seismic wave propagation in a simplified earth model, demonstrating high parallel efficiency for strong scaling to the full size of the *Jaguar* Cray XT5 supercomputer.

1. Introduction

Here we introduce a high-order discontinuous Galerkin (dG) method for wave propagation in coupled elastic–acoustic media. Coupled elastic–acoustic wave propagation phenomena arise in a wide range of scientific and engineering problems. Of particular interest to us are geophysical problems, including seismic exploration and regional and global earthquake-induced wave propagation. Another field in which such problems arise is structural acoustics, in which elastic structures interact with an acoustic fluid within which they are embedded. A common feature of such problems is that they require accurate treatment of waves propagating through elastic–acoustic interfaces. For example, in marine seismology, acoustic waves scatter from the ocean floor and from layers in earth's crust beneath, which is modeled as an elastic medium. When modeling

global seismic wave propagation, earth's outer core is represented as an acoustic fluid, which results in models with several elastic–acoustic interfaces. In regional earthquake wave propagation models, many seismically active regions border oceans, and thus elastic–acoustic interfaces are encountered.

Accurate numerical solution of coupled elastic–acoustic seismic wave propagation problems presents four fundamental difficulties. First, waves are typically propagated over many periods. For example, to propagate seismic waves through the earth at frequencies of interest (up to 1 Hz), waves must be propagated over $\mathcal{O}(10^3)$ wavelengths. This implies a need for high-order methods to control numerical dispersion and dissipation errors [1,2]. Second, maintaining high-order accuracy in the numerical treatment of interfaces requires care. Third, in many problems of interest, the size of bodies excited by acoustic or elastic waves is large relative to the wavelengths of interest, leading to a large number of unknowns necessary to resolve the wavelengths. For example, to propagate a 0.5 Hz wave through the earth using 6 points per wavelength requires more than 10^{11} degrees of freedom, and approximately 10^5 time steps. Clearly, such problems require efficient and scalable implementations on large parallel supercomputers. Fourth, many geophysical problems feature complex geometries and strong contrasts in wave speeds, for example at ocean-crust boundaries. These features present difficulty for contemporary mesh generation algorithms, both in the requirement to conform to interfaces, as well as the need for rapid change in mesh size. The availability of a discretization method that accommodates h-adaptive non-conforming meshes (i.e., those containing adjacent elements of differing size) greatly simplifies mesh generation for such geophysical problems [3]. Moreover, it greatly facilitates dynamic solution adaptivity, for example to track propagating wavefronts or earthquake rupture dynamics.

The four challenges listed above have lead us to consider a high-order dG discretization for the first-order form of the elastic–acoustic wave equations. The dG method is based on discontinuous basis functions, permitting h-non-conforming meshes and greatly simplifying parallel data structures and parallel implementation. Furthermore, the first-order form of the elastic wave equation permits solution of coupled elastic–acoustic wave propagation within a single, unified framework; the acoustic fluid results simply by setting the shear modulus to zero. Discontinuous Galerkin is a natural discretization for hyperbolic conservation laws, which result from the first-order form. In combination with an appropriate numerical flux for the material interfaces, one obtains a stable and arbitrarily high-order accurate method for wave propagation through elastic–acoustic interfaces.

A large body of work exists on numerical methods for elastic and acoustic wave propagation involving elastic–acoustic interfaces. Since our focus is on high-order methods for such problems, here we will review the pertinent literature on this subject. Numerical methods for the elastic wave equation may be based on the formulation of the problem as a system of first-order partial differential equations (in terms of displacement–stress, velocity–stress, or velocity–strain) or as a second-order system (in displacements).

The accurate solution of wave propagation problems with interfaces is a challenging problem for finite difference methods, e.g., [4–6]. Recent work on the stable imposition of free-surface boundary conditions for a second-order formulation can be found in [4]. Another approach, belonging to a broader family of interface methods, handles both free surfaces [5] and elastic–acoustic interfaces [6] in a way, conjectured by the authors, that allows high-order accuracy. Despite the promise of such methods, we prefer methods that do not suffer a growth in stencil size as the order of the approximation increases. This is important for limiting the volume of communication associated with unknowns shared across processors in parallel implementations. Compact finite difference methods do not suffer such a growth; however they have yet to be developed for the coupled elastic–acoustic wave propagation problems we target.

The finite volume method applied to a first-order system has been extended to elastic–acoustic interfaces for control volumes aligned to material interfaces, e.g., [7,8]. However, high-order accurate versions of these methods have yet to be developed.

Finite element and spectral element methods are based typically on the second-order form of wave equations. In this case, the elastic–acoustic interaction is effected by coupling the respective wave equations through appropriate interface conditions. To resolve the coupling, a predictor–multicorrector iteration at each time step has been used [9,10], which increases the computational cost for each time step. A computationally more efficient time-stepping method for global seismic wave propagation is proposed in [11] and extended in [12]. The approach uses a second-order accurate Newmark time integration, in which a time step is first performed in the acoustic fluid and then in the elastic medium using interface values based on the fluid solution.

In contrast to continuous finite element discretizations, dG methods impose continuity between elements only weakly through a numerical flux. Discontinuous Galerkin methods have been employed for second-order wave equations, in both the acoustic and elastodynamic settings. We refer to [13–16] for a review of these methods. For the first-order form, at least two approaches have been proposed. In [17], a velocity–stress formulation in conservative form is employed for the elastic wave equation. Combining a central numerical flux with a leap-frog time discretization results in an energy-conserving method. Alternatively, in [18,19], a non-conservative velocity–stress formulation with an upwind numerical flux using material properties from one side of an (acoustic–acoustic, elastic–elastic, or elastic–acoustic) interface is used.

The discontinuous Galerkin method we develop here is based on a velocity–strain formulation of the coupled elastic–acoustic wave equations. As mentioned above, this allows the acoustic and elastic wave equations to be expressed in conservative form within the same framework (an acoustic medium is a special case of an elastic medium with zero shear modulus). Based on the conservative form, we derive an upwind numerical flux by solving the exact Riemann problem with material discontinuities [20,21]. This is in contrast with the upwind numerical flux employed in [19], which solves the

Riemann problem taking material properties from one side of the interface only. To prove consistency, we show that it is critical to take into account material discontinuities in the numerical flux at elastic–acoustic interfaces. We prove stability of the proposed dG method in the presence of material discontinuities (including elastic–acoustic interfaces) and stress-free boundary conditions. While our derivation is based on a velocity–strain formulation, we show that the resulting method is closely related to a velocity–stress method.

Our implementation of the proposed dG method features hexahedral elements with a basis composed of tensor products of one-dimensional Lagrange polynomials. Furthermore, the numerical integration points coincide with the basis function nodes; here, we use the Legendre–Gauss–Lobatto points. We use curvilinear *h*-adapted non-conforming hexahedral element meshes, where care is taken to ensure constant-state preservation [22]. This set of choices is often referred to as a discontinuous Galerkin spectral element method [23].

We present comparisons between numerical and analytical solutions for a series of classical interface problems and show that our dG method exhibits spectral rates of convergence in each case. We provide the exact solution for each problem and sufficient information to reproduce the test problems. In particular, Rayleigh and Lamb wave problems are presented to verify the implementation of stress-free boundary conditions. Using solutions to Scholte and Stoneley wave problems, we study the behavior of the method for elastic–acoustic and elastic–elastic interfaces. Convergence rates for elastic–acoustic interfaces are further verified in a Snell's Law problem, in which a plane wave is reflected and transmitted at the interface. Finally, in addition to the problems that demonstrate the accuracy of our dG method, we include a preliminary study of scalability of the parallel implementation for large-scale seismic wave propagation in a simplified earth model, demonstrating high parallel efficiency for strong scaling to the full size of the *Jaguar* Cray XT5 supercomputer.

2. Wave propagation in coupled elastic–acoustic media

To formulate the coupled elastic–acoustic wave propagation problem, we assume a deformation $\boldsymbol{\varphi}(\boldsymbol{x}, t)$ that maps a point $\boldsymbol{x}$ from a reference body B to a point $\boldsymbol{x}'$ in the deformed body B' at a given instant in time t. The displacement field $\boldsymbol{u}$ of a material point is a vector pointing from the original location in B to its location in B' given by

$$\boldsymbol{u}(\boldsymbol{x}, t) = \boldsymbol{\varphi}(\boldsymbol{x}, t) - \boldsymbol{x}.$$

Under the assumption of small deformations, the strain tensor $\boldsymbol{E}$ is defined by

$$\boldsymbol{E} = \text{sym}(\nabla \boldsymbol{u}) = \frac{1}{2}(\nabla \boldsymbol{u} + \nabla \boldsymbol{u}^T),$$

where $\text{sym}(\cdot)$ is the mapping from second-order tensors to their symmetric part. In linear elasticity the deformation is assumed to be small such that a linear constitutive relation can be assumed between the strain tensor $\boldsymbol{E}$ and the Cauchy stress tensor $\boldsymbol{S}$ described by the fourth-order constitutive tensor $\mathbf{C}$,

$$\boldsymbol{S} = \mathbf{C}\boldsymbol{E}.$$

The linear elastic wave equation in the body B can be written as the first-order system

$$\frac{\partial \boldsymbol{E}}{\partial t} = \frac{1}{2}(\nabla \boldsymbol{v} + \nabla \boldsymbol{v}^T), \tag{1a}$$

$$\rho \frac{\partial \boldsymbol{v}}{\partial t} = \nabla \cdot (\mathbf{C}\boldsymbol{E}) + \boldsymbol{f}, \tag{1b}$$

where ρ, $\boldsymbol{v}$, and f are mass density, velocity, and body force per unit volume, respectively. For an isotropic medium the constitutive relation can be formulated in terms of the two Lamé parameters λ and μ, and the elastodynamic equations read

$$\frac{\partial \boldsymbol{E}}{\partial t} = \frac{1}{2}(\nabla \boldsymbol{v} + \nabla \boldsymbol{v}^T), \tag{2a}$$

$$\rho \frac{\partial \boldsymbol{v}}{\partial t} = \nabla \cdot (\lambda \text{tr}(\boldsymbol{E})\boldsymbol{I} + 2\mu \boldsymbol{E}) + \boldsymbol{f}, \tag{2b}$$

where $\boldsymbol{I}$ is the second-order identity tensor and $\text{tr}(\boldsymbol{T})$ is the trace of a tensor $\boldsymbol{T}$. In addition to wave propagation in elastic solids, we are also interested in waves propagating in acoustic fluids, and in particular in coupled heterogeneous elastic–acoustic media. In acoustic fluids, wave propagation is described by the acoustic wave equation, which can be written in velocity–strain form by setting μ to zero,

$$\frac{\partial \boldsymbol{E}}{\partial t} = \frac{1}{2}(\nabla \boldsymbol{v} + \nabla \boldsymbol{v}^T), \tag{3a}$$

$$\rho \frac{\partial \boldsymbol{v}}{\partial t} = \nabla \cdot (\lambda \text{tr}(\boldsymbol{E})\boldsymbol{I}) + \boldsymbol{f}, \tag{3b}$$

which implies that the stress tensor reduces to a scalar pressure.

For well-posedness of the system, velocity and strain initial conditions in B and boundary conditions on ∂B need to be specified. Throughout this article we assume the initial conditions

$$\boldsymbol{v}(\boldsymbol{x},0) = \boldsymbol{v}_0(\boldsymbol{x}), \quad \boldsymbol{E}(\boldsymbol{x},0) = \boldsymbol{E}_0(\boldsymbol{x}),$$

and boundary conditions on the traction such that

$$\boldsymbol{Sn} = \boldsymbol{t}_{bc} \quad \text{on } \partial B, \tag{4}$$

where $\boldsymbol{n}$ is the outward unit normal at the boundary ∂B of the body B and the traction $\boldsymbol{t}_{bc}$ is prescribed. Rewritten in terms of strain this boundary condition becomes

$$(\boldsymbol{CE})\boldsymbol{n} = \boldsymbol{t}_{bc} \quad \text{on } \partial B.$$

At an interface $\varGamma$ between two elastic media, the velocity, $\boldsymbol{v}$, and the traction, $\boldsymbol{Sn}$, are continuous, i.e.,

$$\boldsymbol{v}^+ = \boldsymbol{v}^- \quad \boldsymbol{x} \in \varGamma, \tag{5a}$$
$$\boldsymbol{S}^+\boldsymbol{n} = \boldsymbol{S}^-\boldsymbol{n} \quad \boldsymbol{x} \in \varGamma. \tag{5b}$$

For an elastic–acoustic or acoustic–acoustic interface, the normal component of the velocity, $\boldsymbol{n}\cdot\boldsymbol{v}$, and the traction, $\boldsymbol{Sn}$ (which reduces to the pressure in the fluid) are continuous, i.e.,

$$\boldsymbol{n} \cdot \boldsymbol{v}^+ = \boldsymbol{n} \cdot \boldsymbol{v}^- \quad \boldsymbol{x} \in \varGamma, \tag{6a}$$
$$\boldsymbol{S}^+\boldsymbol{n} = \boldsymbol{S}^-\boldsymbol{n} \quad \boldsymbol{x} \in \varGamma. \tag{6b}$$

For a vector $\boldsymbol{w}$ and a second-order tensor $\boldsymbol{T}$, the outward (denoted with superscript "+") and inward (denoted with superscript "-") limits in direction $\boldsymbol{n}$ are given by

$$\boldsymbol{w}^+(\boldsymbol{x},t) := \lim_{\tau\to 0^+} \boldsymbol{w}(\boldsymbol{x}+\tau\boldsymbol{n},t), \quad \boldsymbol{w}^-(\boldsymbol{x},t) := \lim_{\tau\to 0^-} \boldsymbol{w}(\boldsymbol{x}+\tau\boldsymbol{n},t),$$
$$\boldsymbol{T}^+(\boldsymbol{x},t) := \lim_{\tau\to 0^+} \boldsymbol{T}(\boldsymbol{x}+\tau\boldsymbol{n},t), \quad \boldsymbol{T}^-(\boldsymbol{x},t) := \lim_{\tau\to 0^-} \boldsymbol{T}(\boldsymbol{x}+\tau\boldsymbol{n},t).$$

We use numerical subscripts to denote components of vectors and tensors, e.g., $\boldsymbol{u} = (u_1,u_2,u_3)^T$, given in the basis $\{\boldsymbol{e}_1,\boldsymbol{e}_2,\boldsymbol{e}_3\}$. To formulate the discontinuous Galerkin method, we first rewrite the elastic wave equation (1) in conservative form. This is accomplished using the definitions

$$\nabla \cdot \boldsymbol{S} = \sum_{j=1}^{3}\sum_{i=1}^{3} \frac{\partial S_{ij}}{\partial x_j}\boldsymbol{e}_i = \sum_{j=1}^{3}\frac{\partial}{\partial x_j}\sum_{i=1}^{3}S_{ij}\boldsymbol{e}_i = \sum_{j=1}^{3}\frac{\partial}{\partial x_j}\boldsymbol{Se}_j,$$

$$\nabla\boldsymbol{v} = \sum_{j=1}^{3}\sum_{i=1}^{3}\frac{\partial v_i}{\partial x_j}\boldsymbol{e}_i\otimes\boldsymbol{e}_j = \sum_{j=1}^{3}\frac{\partial}{\partial x_j}\left(\sum_{i=1}^{3}v_i\boldsymbol{e}_i\right)\otimes\boldsymbol{e}_j = \sum_{j=1}^{3}\frac{\partial}{\partial x_j}\boldsymbol{v}\otimes\boldsymbol{e}_j,$$

$$\nabla\boldsymbol{v}^T = \sum_{j=1}^{3}\sum_{i=1}^{3}\frac{\partial v_j}{\partial x_i}\boldsymbol{e}_i\otimes\boldsymbol{e}_j = \sum_{i=1}^{3}\frac{\partial}{\partial x_i}\boldsymbol{e}_i\otimes\left(\sum_{j=1}^{3}v_j\boldsymbol{e}_j\right) = \sum_{i=1}^{3}\frac{\partial}{\partial x_i}\boldsymbol{e}_i\otimes\boldsymbol{v},$$

where the tensor $\boldsymbol{a}\otimes\boldsymbol{b}$ is the dyadic product of vectors $\boldsymbol{a}$ and $\boldsymbol{b}$. This allows us to state the conservative form in the space $\boldsymbol{V} := V_{\text{sym}}^{3\times 3} \oplus V^3$, where V denotes a space of sufficiently smooth functions defined on B, as follows,

$$\boldsymbol{Q}\frac{\partial\boldsymbol{q}}{\partial t} + \nabla \cdot (\mathfrak{F}\boldsymbol{q}) = \boldsymbol{g}, \tag{7}$$

where

$$\boldsymbol{q} = \begin{pmatrix} \boldsymbol{E} \\ \boldsymbol{v} \end{pmatrix} \in \boldsymbol{V}, \quad \boldsymbol{Q} = \begin{pmatrix} \mathsf{I} & 0 \\ 0 & \rho\boldsymbol{I} \end{pmatrix}, \quad \boldsymbol{g} = \begin{pmatrix} 0 \\ \boldsymbol{f} \end{pmatrix} \in \boldsymbol{V}$$

and the action of the flux operator $\mathfrak{F}$ on the strain–velocity unknowns $\boldsymbol{q}$ is defined by

$$(\mathfrak{F}\boldsymbol{q})_i = \begin{pmatrix} -\frac{1}{2}(\boldsymbol{v}\otimes\boldsymbol{e}_i + \boldsymbol{e}_i\otimes\boldsymbol{v}) \\ -(\boldsymbol{CE})\boldsymbol{e}_i \end{pmatrix} \in \boldsymbol{V} \quad \text{for } i = 1,2,3,$$

with I denoting the fourth-order identity tensor and 0 denoting zero tensors of appropriate sizes.

To solve (7) with a discontinuous Galerkin method, the domain B is partitioned into N_{el} elements aligned with material discontinuities such that $B \approx B^{N_{el}} = \bigcup_{e=1}^{N_{el}} \mathsf{D}^e$. Then (7) is multiplied by a test function $\boldsymbol{p} \in \boldsymbol{V}$ using the following inner product for the direct sum space $\boldsymbol{V}$:

$$\boldsymbol{q} \cdot \boldsymbol{p} = \boldsymbol{E} : (\boldsymbol{CH}) + \boldsymbol{v} \cdot \boldsymbol{w}, \quad \text{with } \boldsymbol{p} = \begin{pmatrix} \boldsymbol{H} \\ \boldsymbol{w} \end{pmatrix}. \tag{8}$$

The use of $\boldsymbol{C}$ in this inner product eliminates redundant variables when acoustic waves are treated as a special case of elastic waves in a unified elastic–acoustic formulation. The dG formulation on an element D^e is obtained by integration by parts in space on each element D^e,

$$\int_{D^e} \mathbf{Q} \frac{\partial \boldsymbol{q}}{\partial t} \cdot \boldsymbol{p} dx + \int_{D^e} (\nabla \cdot \mathfrak{F}\boldsymbol{q}) \cdot \boldsymbol{p} dx + \int_{\partial D^e} (\boldsymbol{n} \cdot ((\mathfrak{F}\boldsymbol{q})^* - \mathfrak{F}^- \boldsymbol{q}^-)) \cdot \boldsymbol{p} dx = \int_{D^e} \boldsymbol{g} \cdot \boldsymbol{p} dx \quad \text{for all } \boldsymbol{p} \in \boldsymbol{V}, \tag{9}$$

where $(\mathfrak{F}\boldsymbol{q})^*$ is the numerical flux across element interfaces. Note that at this point we have not assumed a particular spatial discretization for $\boldsymbol{q}$ and $\boldsymbol{p}$; a specific choice will be discussed in Section 5. In the next section, we choose an upwind numerical flux, defined as the flux of the solution of the Riemann problem at the interface. The solution of this Riemann problem is detailed next.

3. Upwind numerical flux

In this section we compute the upwind numerical flux for the three-dimensional isotropic coupled elastic and acoustic wave equations (2). Existing work on the upwind numerical flux for the two-dimensional elastic wave equation includes [7,21] using a velocity–stress formulation and [7] using a velocity–strain formulation. Note that the numerical flux used in [24,19] takes into account material parameters from one side of the interface only; see Section 4.1 for a discussion of this simplification. The subsequent exact solution of the Riemann problem combines material parameters from both sides of the interface following standard techniques; see for example [20,21]. As can be seen below, the computation in three dimensions is technical and additional steps are needed to rigorously derive the flux for elastic–elastic, acoustic–acoustic, and elastic–acoustic interfaces within a unified formulation. We conclude this section with a method to impose stress-free boundary conditions weakly through the numerical flux. This allows a unified numerical treatment of both intra-element and boundary faces.

3.1. Flux across elastic–elastic interfaces

We first focus on the elastic–elastic Riemann problem for (7). To simplify notation, we use the isomorphism between the direct sum space $\boldsymbol{V} = V_{\text{sym}}^{3 \times 3} \oplus V^3$ and V^9 in the following derivation. Under this isomorphism, the tensors $\boldsymbol{n} \cdot \mathfrak{F}$ and $\boldsymbol{Q}$ are represented by the matrices A and Q (as defined below) and $\boldsymbol{q}$, $\boldsymbol{p}$ and $\boldsymbol{g}$ are denoted by $\mathbf{q}$, $\mathbf{p}$, $\mathbf{g} \in V^9$. Then, the elastic wave equation can be written as

$$Q \frac{\partial \mathbf{q}}{\partial t} + \frac{\partial A_1 \mathbf{q}}{\partial x_1} + \frac{\partial A_2 \mathbf{q}}{\partial x_2} + \frac{\partial A_3 \mathbf{q}}{\partial x_3} = \mathbf{g}, \tag{10}$$

where

$$\mathbf{q} = (\begin{matrix} E_{11} & E_{22} & E_{33} & E_{12} & E_{23} & E_{13} & v_1 & v_2 & v_3 \end{matrix})^T,$$

$$\mathbf{g} = (\begin{matrix} 0 & 0 & 0 & 0 & 0 & 0 & f_1 & f_2 & f_3 \end{matrix})^T,$$

$$Q = \text{diag}(1, 1, 1, 1, 1, 1, \rho, \rho, \rho),$$

$$A = n_1 A_1 + n_2 A_2 + n_3 A_3 = \begin{pmatrix} 0 & A_{12} \\ A_{21} & 0 \end{pmatrix}$$

and

$$A_{12} = - \begin{pmatrix} n_1 & 0 & 0 \\ 0 & n_2 & 0 \\ 0 & 0 & n_3 \\ \frac{n_2}{2} & \frac{n_1}{2} & 0 \\ 0 & \frac{n_3}{2} & \frac{n_2}{2} \\ \frac{n_3}{2} & 0 & \frac{n_1}{2} \end{pmatrix},$$

$$A_{21} = - \begin{pmatrix} (\lambda + 2\mu)n_1 & \lambda n_1 & \lambda n_1 & 2\mu n_2 & 0 & 2\mu n_3 \\ \lambda n_2 & (\lambda + 2\mu)n_2 & \lambda n_2 & 2\mu n_1 & 2\mu n_3 & 0 \\ \lambda n_3 & \lambda n_3 & (\lambda + 2\mu)n_3 & 0 & 2\mu n_2 & 2\mu n_1 \end{pmatrix}.$$

Above and in the remainder of this section, $\boldsymbol{n} := \boldsymbol{n}^-$ denotes the outward interface unit normal vector. The flux in the normal direction is then $A\mathbf{q}$. We augment $\boldsymbol{n}$ with tangential vectors $\boldsymbol{s}$ and $\boldsymbol{t}$ such that $\{\boldsymbol{n}, \boldsymbol{s}, \boldsymbol{t}\}$ is an orthonormal basis. Note that $\boldsymbol{s}$ and $\boldsymbol{t}$ are only used to facilitate the derivation and do not appear in the final form of the numerical flux. We simplify the following calculations by introducing the matrix T, which is the coordinate representation of the transformation from the interface basis $\{\boldsymbol{n}, \boldsymbol{s}, \boldsymbol{t}\}$ to the physical basis $\{\boldsymbol{e}_1, \boldsymbol{e}_2, \boldsymbol{e}_3\}$ for $\boldsymbol{E}$ and $\boldsymbol{v}$; we refer to [25] for details about general transformations of vectors and tensors. From the definition of T it follows that

$$T^{-1}AT = A_1 \quad \text{and} \quad T^{-1}Q^{-1}AT = Q^{-1}A_1. \tag{11}$$

Denoting the coordinates in the interface basis with a prime we have

$$\mathbf{q}' = T^{-1}\mathbf{q} = (\mathbf{n} \cdot E\mathbf{n} \quad \mathbf{s} \cdot E\mathbf{s} \quad \mathbf{t} \cdot E\mathbf{t} \quad \mathbf{s} \cdot E\mathbf{n} \quad \mathbf{t} \cdot E\mathbf{s} \quad \mathbf{t} \cdot E\mathbf{n} \quad \mathbf{n} \cdot \mathbf{v} \quad \mathbf{s} \cdot \mathbf{v} \quad \mathbf{t} \cdot \mathbf{v})^T.$$

For the solution of the Riemann problem at the interface, we consider an interface between two homogeneous media with properties $\{\lambda^-, \mu^-, \rho^-\}$ in the inward direction of $\mathbf{n}$ and $\{\lambda^+, \mu^+, \rho^+\}$ in the outward direction of $\mathbf{n}$. Then, the Riemann problem is to solve (10) for the given piecewise constant medium with the initial condition

$$\mathbf{q}_0(\mathbf{x}) = \begin{cases} \mathbf{q}^- & \text{if } \mathbf{n} \cdot \mathbf{x} < 0, \\ \mathbf{q}^+ & \text{if } \mathbf{n} \cdot \mathbf{x} > 0. \end{cases}$$

To determine the characteristics of this hyperbolic system we need the decomposition

$$Q^{-1}A = RAR^{-1}, \tag{12}$$

where the columns of R, denoted as $\mathbf{r}_j$ for the jth column, are the eigenvectors of $Q^{-1}A$ and Λ is the diagonal matrix

$$\Lambda = diag(-c_p, -c_s, -c_s, 0, 0, 0, c_s, c_s, c_p),$$

with

$$c_p = \sqrt{\frac{\lambda + 2\mu}{\rho}} \quad \text{and} \quad c_s = \sqrt{\frac{\mu}{\rho}}$$

denoting the principal wave speeds in the system. Transforming (12) into the interface basis and using (11) results in

$$Q^{-1}A_1 = T^{-1}Q^{-1}AT = T^{-1}RAR^{-1}T = R'\Lambda(R')^{-1},$$

where

$$R' = T^{-1}R.$$

Thus we obtain $\mathbf{r}_j = T\mathbf{r}'_j$, where $\mathbf{r}'_j$ is the jth column of

$$R' = \begin{pmatrix} 1 & 0 & 0 & -\lambda & 0 & -\lambda & 0 & 0 & 1 \\ 0 & 0 & 0 & \lambda + 2\mu & 0 & 0 & 0 & 0 & 0 \\ 0 & 0 & 0 & 0 & 0 & \lambda + 2\mu & 0 & 0 & 0 \\ 0 & \frac{1}{2} & 0 & 0 & 0 & 0 & 0 & \frac{1}{2} & 0 \\ 0 & 0 & 0 & 0 & 1 & 0 & 0 & 0 & 0 \\ 0 & 0 & \frac{1}{2} & 0 & 0 & 0 & \frac{1}{2} & 0 & 0 \\ c_p & 0 & 0 & 0 & 0 & 0 & 0 & 0 & -c_p \\ 0 & c_s & 0 & 0 & 0 & 0 & 0 & -c_s & 0 \\ 0 & 0 & c_s & 0 & 0 & 0 & -c_s & 0 & 0 \end{pmatrix}.$$

For each wave speed c_i in our system, the Rankine–Hugoniot jump condition is

$$-c_i Q(\mathbf{q}^m - \mathbf{q}^p) + A(\mathbf{q}^m - \mathbf{q}^p) = 0. \tag{13}$$

Here, $\mathbf{q}^m$ is the state in the negative normal direction across the discontinuity traveling at speed c_i and $\mathbf{q}^p$ is the state in the positive normal direction. The matrices Q and A are evaluated in the region where the c_i-wave travels, which is emphasized
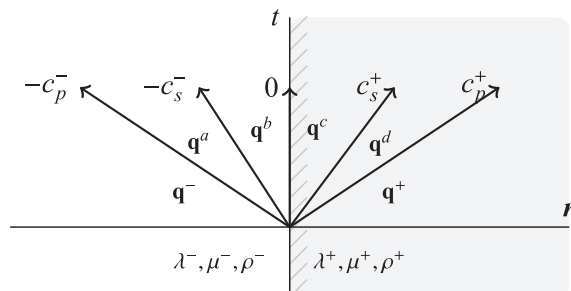

Fig. 1. Sketch illustrating the Ranking–Hugoniot jump conditions in the Riemann problem.

by the superscripts "-" and "+". The Riemann problem has four unknown states $\{\mathbf{q}^a, \mathbf{q}^b, \mathbf{q}^c, \mathbf{q}^d\}$; see Fig. 1. The following Rankine–Hugoniot jump conditions hold for our system:

$$c_p^- Q^- (\mathbf{q}^- - \mathbf{q}^a) + A^- (\mathbf{q}^- - \mathbf{q}^a) \qquad = 0, \tag{14a}$$
$$c_s^- Q^- (\mathbf{q}^a - \mathbf{q}^b) + A^- (\mathbf{q}^a - \mathbf{q}^b) \qquad = 0, \tag{14b}$$
$$A^- \mathbf{q}^b - A^+ \mathbf{q}^c \qquad = 0, \tag{14c}$$
$$-c_s^+ Q^+ (\mathbf{q}^c - \mathbf{q}^d) + A^+ (\mathbf{q}^c - \mathbf{q}^d) \quad = 0, \tag{14d}$$
$$-c_p^+ Q^+ (\mathbf{q}^d - \mathbf{q}^+) + A^+ (\mathbf{q}^d - \mathbf{q}^+) \quad = 0. \tag{14e}$$

Due to the definition of the eigenvalues and eigenvectors of $(Q^-)^{-1} A^-$ and $(Q^+)^{-1} A^+$, we obtain

$$\mathbf{q}^- - \mathbf{q}^a = \alpha_1 \mathbf{r}_1^-,$$
$$\mathbf{q}^a - \mathbf{q}^b = \alpha_2 \mathbf{r}_2^- + \alpha_3 \mathbf{r}_3^-,$$
$$\mathbf{q}^c - \mathbf{q}^d = \alpha_7 \mathbf{r}_7^+ + \alpha_8 \mathbf{r}_8^+,$$
$$\mathbf{q}^d - \mathbf{q}^+ = \alpha_9 \mathbf{r}_9^+,$$

which combined with (14c) yields the system of equations

$$\mathbf{q}^- - \mathbf{q}^b \qquad = \alpha_1 \mathbf{r}_1^- + \alpha_2 \mathbf{r}_2^- + \alpha_3 \mathbf{r}_3^-,$$
$$A^- \mathbf{q}^b - A^+ \mathbf{q}^c = 0,$$
$$\mathbf{q}^c - \mathbf{q}^+ \qquad = \alpha_9 \mathbf{r}_9^+, + \alpha_8 \mathbf{r}_8^+ + \alpha_7 \mathbf{r}_7^+,$$

which we solve for the characteristic coefficients $\boldsymbol{\alpha}$. There is no need to determine α_4, α_5, or α_6 since they correspond to waves with zero speed, which do not contribute to the upwind numerical flux. Transforming the system into the interface coordinates using (11), we obtain

$$T^{-1} \mathbf{q}^- - T^{-1} \mathbf{q}^b \qquad = \alpha_1 (\mathbf{r}_1')^- + \alpha_2 (\mathbf{r}_2')^- + \alpha_3 (\mathbf{r}_3')^-, \tag{15a}$$
$$A_1^- T^{-1} \mathbf{q}^b - A_1^+ T^{-1} \mathbf{q}^c = 0, \tag{15b}$$
$$T^{-1} \mathbf{q}^c - T^{-1} \mathbf{q}^+ \qquad = \alpha_9 (\mathbf{r}_9')^+ + \alpha_8 (\mathbf{r}_8')^+ + \alpha_7 (\mathbf{r}_7')^+. \tag{15c}$$

Eq. (15b) implies that the flux is continuous across interfaces, namely

$$\boldsymbol{v}^b = \boldsymbol{v}^c, \tag{16a}$$
$$\boldsymbol{S}^b \boldsymbol{n} = \boldsymbol{S}^c \boldsymbol{n}, \tag{16b}$$

where

$$\boldsymbol{S}^b = \lambda^- \mathrm{tr}(\boldsymbol{E}^b) \boldsymbol{I} + 2\mu^- \boldsymbol{E}^b, \quad \boldsymbol{S}^c = \lambda^+ \mathrm{tr}(\boldsymbol{E}^c) \boldsymbol{I} + 2\mu^+ \boldsymbol{E}^c.$$

Rewriting the traction interface condition (14c) in terms of strain yields

$$\lambda^- \mathrm{tr}(\boldsymbol{E}^b) + 2\mu^- \boldsymbol{n} \cdot \boldsymbol{E}^b \boldsymbol{n} = \lambda^+ \mathrm{tr}(\boldsymbol{E}^c) + 2\mu^+ \boldsymbol{n} \cdot \boldsymbol{E}^c \boldsymbol{n}.$$

Since the trace is invariant under orthogonal transformations (e.g., [25]), we infer

$$\lambda^- (\boldsymbol{n} \cdot \boldsymbol{E}^b \boldsymbol{n} + \boldsymbol{s} \cdot \boldsymbol{E}^b \boldsymbol{s} + \boldsymbol{t} \cdot \boldsymbol{E}^b \boldsymbol{t}) + 2\mu^- \boldsymbol{n} \cdot \boldsymbol{E}^b \boldsymbol{n} = \lambda^+ (\boldsymbol{n} \cdot \boldsymbol{E}^c \boldsymbol{n} + \boldsymbol{s} \cdot \boldsymbol{E}^c \boldsymbol{s} + \boldsymbol{t} \cdot \boldsymbol{E}^c \boldsymbol{t}) + 2\mu^+ \boldsymbol{n} \cdot \boldsymbol{E}^c \boldsymbol{n}. \tag{17}$$

From the first three rows of (15a) and (15c) and substituting the relations

$$\boldsymbol{n} \cdot \boldsymbol{E}^b \boldsymbol{n} = \boldsymbol{n} \cdot \boldsymbol{E}^- \boldsymbol{n} - \alpha_1, \quad \boldsymbol{s} \cdot \boldsymbol{E}^b \boldsymbol{s} = \boldsymbol{s} \cdot \boldsymbol{E}^- \boldsymbol{s}, \quad \boldsymbol{t} \cdot \boldsymbol{E}^b \boldsymbol{t} = \boldsymbol{t} \cdot \boldsymbol{E}^- \boldsymbol{t},$$
$$\boldsymbol{n} \cdot \boldsymbol{E}^c \boldsymbol{n} = \boldsymbol{n} \cdot \boldsymbol{E}^+ \boldsymbol{n} + \alpha_9, \quad \boldsymbol{s} \cdot \boldsymbol{E}^c \boldsymbol{s} = \boldsymbol{s} \cdot \boldsymbol{E}^+ \boldsymbol{s}, \quad \boldsymbol{t} \cdot \boldsymbol{E}^c \boldsymbol{t} = \boldsymbol{t} \cdot \boldsymbol{E}^+ \boldsymbol{t},$$

into (17), we conclude that

$$(\lambda^- + 2\mu^-)\alpha_1 + (\lambda^+ + 2\mu^+)\alpha_9 = \boldsymbol{n} \cdot (\boldsymbol{S}^- \boldsymbol{n} - \boldsymbol{S}^+ \boldsymbol{n}). \tag{18}$$

Likewise it follows from (16a) that $\boldsymbol{n} \cdot \boldsymbol{v}^b = \boldsymbol{n} \cdot \boldsymbol{v}^c$, which, along with the seventh row of (15a), allows us to obtain a second equation for α_1 and α_9:

$$c_p^- \alpha_1 - c_p^+ \alpha_9 = \boldsymbol{n} \cdot (\boldsymbol{v}^- - \boldsymbol{v}^+). \tag{19}$$

Solving Eq. (18) and (19) we find

$$\alpha_1 = \frac{c_p^+ \boldsymbol{n}^- \cdot [\![\boldsymbol{S}]\!] + (\lambda^+ + 2\mu^+)[\![\boldsymbol{v}]\!]}{c_p^+ (\lambda^- + 2\mu^-) + c_p^- (\lambda^+ + 2\mu^+)},$$
$$\alpha_9 = \frac{c_p^- \boldsymbol{n}^- \cdot [\![\boldsymbol{S}]\!] - (\lambda^- + 2\mu^-)[\![\boldsymbol{v}]\!]}{c_p^+ (\lambda^- + 2\mu^-) + c_p^- (\lambda^+ + 2\mu^+)},$$

where we have introduced $\llbracket \boldsymbol{v} \rrbracket = \boldsymbol{n}^- \cdot \boldsymbol{v}^- + \boldsymbol{n}^+ \cdot \boldsymbol{v}^+$ and $\llbracket \boldsymbol{S} \rrbracket = \boldsymbol{S}^- \boldsymbol{n}^- + \boldsymbol{S}^+ \boldsymbol{n}^+$. Rows 4 and 8 in (15a) and (15c) result in the equations

$$\mu^- \alpha_2 + \mu^+ \alpha_8 = \boldsymbol{s} \cdot (\boldsymbol{S}^- \boldsymbol{n} - \boldsymbol{S}^+ \boldsymbol{n}),$$
$$c_s^- \alpha_2 - c_s^+ \alpha_8 = \boldsymbol{s} \cdot (\boldsymbol{v}^- - \boldsymbol{v}^+).$$

Similarly, rows 6 and 9 in (15a) and (15c) yield

$$\mu^- \alpha_3 + \mu^+ \alpha_7 = \boldsymbol{t} \cdot (\boldsymbol{S}^- \boldsymbol{n} - \boldsymbol{S}^+ \boldsymbol{n}),$$
$$c_s^- \alpha_3 - c_s^+ \alpha_7 = \boldsymbol{t} \cdot (\boldsymbol{v}^- - \boldsymbol{v}^+).$$

The solution of these equations is

$$\alpha_2 = \frac{1}{\mu^+ c_s^- + \mu^- c_s^+} \left(c_s^+ \boldsymbol{s} \cdot (\boldsymbol{S}^- \boldsymbol{n} - \boldsymbol{S}^+ \boldsymbol{n}) + \mu^+ \boldsymbol{s} \cdot (\boldsymbol{v}^- - \boldsymbol{v}^+) \right),$$

$$\alpha_3 = \frac{1}{\mu^+ c_s^- + \mu^- c_s^+} \left(c_s^+ \boldsymbol{t} \cdot (\boldsymbol{S}^- \mathrm{n} - \boldsymbol{S}^+ \boldsymbol{n}) + \mu^+ \boldsymbol{t} \cdot (\boldsymbol{v}^- - \boldsymbol{v}^+) \right),$$

$$\alpha_7 = \frac{1}{\mu^+ c_s^- + \mu^- c_s^+} \left(c_s^- \boldsymbol{t} \cdot (\boldsymbol{S}^- \mathrm{n} - \boldsymbol{S}^+ \boldsymbol{n}) - \mu^- \boldsymbol{t} \cdot (\boldsymbol{v}^- - \boldsymbol{v}^+) \right),$$

$$\alpha_8 = \frac{1}{\mu^+ c_s^- + \mu^- c_s^+} \left(c_s^- \boldsymbol{s} \cdot (\boldsymbol{S}^- \mathrm{n} - \boldsymbol{S}^+ \boldsymbol{n}) - \mu^- \boldsymbol{s} \cdot (\boldsymbol{v}^- - \boldsymbol{v}^+) \right).$$

Thus, we define the upwind numerical flux in the normal direction $(A\mathbf{q})^*$ as

$$(A\mathbf{q})^* = A^- \mathbf{q}^- + \alpha_1 c_p^- Q^- \mathbf{r}_1^- + \alpha_2 c_s^- Q^- \mathbf{r}_2^- + \alpha_3 c_s^- Q^- \mathbf{r}_3^- = A^+ \mathbf{q}^+ + \alpha_9 c_p^+ Q^+ \mathbf{r}_9^+ + \alpha_8 c_s^+ Q^+ \mathbf{r}_8^+ + \alpha_7 c_s^+ Q^+ \mathbf{r}_7^+. \tag{20}$$

Using the fact that $\mathbf{r}_1$, $\mathbf{r}_2$, $\mathbf{r}_3$ correspond to

$$\boldsymbol{r}_1^- = \begin{pmatrix} \boldsymbol{n} \otimes \boldsymbol{n} \\ c_p^- \boldsymbol{n} \end{pmatrix}, \quad \boldsymbol{r}_2^- = \begin{pmatrix} \mathrm{sym}(\boldsymbol{s} \otimes \boldsymbol{n}) \\ c_s^- \boldsymbol{s} \end{pmatrix}, \quad \boldsymbol{r}_3^- = \begin{pmatrix} \mathrm{sym}(\boldsymbol{t} \otimes \boldsymbol{n}) \\ c_s^- \boldsymbol{t} \end{pmatrix},$$

and using, for a vector $\boldsymbol{a}$, the vector–tensor identities

$$(\boldsymbol{s} \cdot \boldsymbol{a})\boldsymbol{s} + (\boldsymbol{t} \cdot \boldsymbol{a})\boldsymbol{t} = -\boldsymbol{n} \times (\boldsymbol{n} \times \boldsymbol{a}),$$
$$(\boldsymbol{s} \cdot \boldsymbol{a})\mathrm{sym}(\boldsymbol{s} \otimes \boldsymbol{n}) + (\boldsymbol{t} \cdot \boldsymbol{a})\mathrm{sym}(\boldsymbol{t} \otimes \boldsymbol{n}) = -\mathrm{sym}(\boldsymbol{n} \otimes (\boldsymbol{n} \times (\boldsymbol{n} \times \boldsymbol{a}))),$$

we obtain the upwind numerical flux for an elastic–elastic interface, where we use (20) and state the flux in the product space $\boldsymbol{V}$:

$$
\begin{aligned}
(\mathfrak{F}\boldsymbol{q})^* = {} & \mathfrak{F}^- \boldsymbol{q}^- + \frac{c_p^- c_p^+ \boldsymbol{n} \cdot \llbracket \boldsymbol{S} \rrbracket + c_p^- (\lambda^+ + 2\mu^+) \llbracket \boldsymbol{v} \rrbracket}{c_p^+ (\lambda^- + 2\mu^-) + c_p^- (\lambda^+ + 2\mu^+)} \begin{pmatrix} \boldsymbol{n} \otimes \boldsymbol{n} \\ \rho^- c_p^- \boldsymbol{n} \end{pmatrix} + \left(\frac{c_s^- c_s^+}{\mu^+ c_s^- + \mu^- c_s^+} \boldsymbol{s} \cdot \llbracket \boldsymbol{S} \rrbracket + \frac{c_s^- \mu^+}{\mu^+ c_s^- + \mu^- c_s^+} \boldsymbol{s} \cdot [\boldsymbol{v}] \right) \begin{pmatrix} \mathrm{sym}(\boldsymbol{s} \otimes \boldsymbol{n}) \\ \rho^- c_s^- \boldsymbol{s} \end{pmatrix} \\
& + \left(\frac{c_s^- c_s^+}{\mu^+ c_s^- + \mu^- c_s^+} \boldsymbol{t} \cdot \llbracket \boldsymbol{S} \rrbracket + \frac{c_s^- \mu^+}{\mu^+ c_s^- + \mu^- c_s^+} \boldsymbol{t} \cdot [\boldsymbol{v}] \right) \begin{pmatrix} \mathrm{sym}(\boldsymbol{t} \otimes \boldsymbol{n}) \\ \rho^- c_s^- \boldsymbol{t} \end{pmatrix} = \mathfrak{F}^- \boldsymbol{q}^- + \frac{c_p^- c_p^+ \boldsymbol{n} \cdot \llbracket \boldsymbol{S} \rrbracket + c_p^- (\lambda^+ + 2\mu^+) \llbracket \boldsymbol{v} \rrbracket}{c_p^+ (\lambda^- + 2\mu^-) + c_p^- (\lambda^+ + 2\mu^+)} \begin{pmatrix} \boldsymbol{n} \otimes \boldsymbol{n} \\ \rho^- c_p^- \boldsymbol{n} \end{pmatrix} \\
& - \frac{c_s^- c_s^+}{\mu^+ c_s^- + \mu^- c_s^+} \begin{pmatrix} \mathrm{sym}(\boldsymbol{n} \otimes (\boldsymbol{n} \times (\boldsymbol{n} \times \llbracket \boldsymbol{S} \rrbracket))) \\ \rho^- c_s^- \boldsymbol{n} \times (\boldsymbol{n} \times \llbracket \boldsymbol{S} \rrbracket) \end{pmatrix} - \frac{c_s^- \mu^+}{\mu^+ c_s^- + \mu^- c_s^+} \begin{pmatrix} \mathrm{sym}(\boldsymbol{n} \otimes (\boldsymbol{n} \times (\boldsymbol{n} \times [\boldsymbol{v}]))) \\ \rho^- c_s^- \boldsymbol{n} \times (\boldsymbol{n} \times [\boldsymbol{v}]) \end{pmatrix}, \\
= {} & \mathfrak{F}^- \boldsymbol{q}^- + \frac{\boldsymbol{n} \cdot \llbracket \boldsymbol{S} \rrbracket + \rho^+ c_p^+ \llbracket \boldsymbol{v} \rrbracket}{\rho^+ c_p^+ + \rho^- c_p^-} \begin{pmatrix} \boldsymbol{n} \otimes \boldsymbol{n} \\ \rho^- c_p^- \boldsymbol{n} \end{pmatrix} - \frac{1}{\rho^- c_s^- + \rho^+ c_s^+} \begin{pmatrix} \mathrm{sym}(\boldsymbol{n} \otimes (\boldsymbol{n} \times (\boldsymbol{n} \times \llbracket \boldsymbol{S} \rrbracket))) \\ \rho^- c_s^- \boldsymbol{n} \times (\boldsymbol{n} \times \llbracket \boldsymbol{S} \rrbracket) \end{pmatrix} \\
& - \frac{\rho^+ c_s^+}{\rho^- c_s^- + \rho^+ c_s^+} \begin{pmatrix} \mathrm{sym}(\boldsymbol{n} \otimes (\boldsymbol{n} \times (\boldsymbol{n} \times [\boldsymbol{v}]))) \\ \rho^- c_s^- \boldsymbol{n} \times (\boldsymbol{n} \times [\boldsymbol{v}]) \end{pmatrix},
\end{aligned}
$$

with the definition $[\boldsymbol{v}] = \boldsymbol{v}^- - \boldsymbol{v}^+$.

3.2. Flux across acoustic–acoustic interfaces

Acoustic–acoustic interfaces are characterized by $\mu^- = \mu^+ = 0$, which implies that (10) is a weakly hyperbolic system for which we cannot directly apply the method used in the elastic–elastic case discussed above; see [21, Chapter 16.3.1]. Instead, we reduce the Riemann problem to solving for

$$\hat{\mathbf{q}} = \begin{pmatrix} E_{11} & E_{22} & E_{33} & v_1 & v_2 & v_3 \end{pmatrix}^T. \tag{21}$$

From the solution of this restricted but strongly hyperbolic system, E_{12}, E_{23}, and E_{13} can be inferred by exploiting the relations

$$\frac{\partial E_{12}}{\partial t} = \frac{1}{2}\left(\frac{\partial v_1}{\partial x_2} + \frac{\partial v_2}{\partial x_1}\right), \quad \frac{\partial E_{23}}{\partial t} = \frac{1}{2}\left(\frac{\partial v_2}{\partial x_3} + \frac{\partial v_3}{\partial x_2}\right), \quad \frac{\partial E_{13}}{\partial t} = \frac{1}{2}\left(\frac{\partial v_1}{\partial x_3} + \frac{\partial v_3}{\partial x_1}\right).$$

This procedure yields the upwind numerical flux in the normal direction for acoustic–acoustic interfaces

$$(\mathfrak{F}\boldsymbol{q})^* = \mathfrak{F}^- \boldsymbol{q}^- + \frac{\boldsymbol{n}\cdot[\![\boldsymbol{S}]\!] + \rho^+ c_p^+ [\![\boldsymbol{v}]\!]}{\rho^+ c_p^+ + \rho^- c_p^-}\left(\begin{array}{c}\boldsymbol{n}\otimes\boldsymbol{n}\\\rho^- c_p^- \boldsymbol{n}\end{array}\right).$$

3.3. Flux across elastic–acoustic and acoustic–elastic interfaces

Let us first concentrate on finding the flux for an elastic–acoustic interface (i.e., $\mu^- \neq 0$ and $\mu^+ = 0$). In this situation the solution of the Riemann problem satisfies the following Rankine–Hugoniot jump conditions

$$c_p^- Q^-(\boldsymbol{q}^- - \boldsymbol{q}^a) + A^-(\boldsymbol{q}^- - \boldsymbol{q}^a) = 0,$$
$$c_s^- Q^-(\boldsymbol{q}^a - \boldsymbol{q}^b) + A^-(\boldsymbol{q}^a - \boldsymbol{q}^b) = 0,$$
$$A^- \boldsymbol{q}^b - A^+ \boldsymbol{q}^c = 0,$$
$$-c_p^+ \widehat{Q}^+(\hat{\boldsymbol{q}}^c - \hat{\boldsymbol{q}}^+) + \widehat{A}^+(\hat{\boldsymbol{q}}^c - \hat{\boldsymbol{q}}^+) = 0,$$

where the hat-superscript indicates that we have restricted the operators and vectors to the variables E_{11}, E_{22}, E_{33}, v_1, v_2, and v_3 per (21). In fact, since the flux $A^+ \boldsymbol{q}^c$ involves only the shear stress which we know to be zero in an acoustic region, we may solve this system first and then use the separate set of equations

$$\frac{\partial E_{12}^+}{\partial t} = \frac{1}{2}\left(\frac{\partial v_1^+}{\partial x_2} + \frac{\partial v_2^+}{\partial x_1}\right), \quad \frac{\partial E_{23}^+}{\partial t} = \frac{1}{2}\left(\frac{\partial v_2^+}{\partial x_3} + \frac{\partial v_3^+}{\partial x_2}\right), \quad \frac{\partial E_{13}^+}{\partial t} = \frac{1}{2}\left(\frac{\partial v_1^+}{\partial x_3} + \frac{\partial v_3^+}{\partial x_1}\right)$$

for the acoustic side of the interface. The resulting numerical flux involves an upwind term for the incoming c_p characteristic and boundary conditions for the incoming c_s characteristics such that

$$\boldsymbol{s}\cdot\boldsymbol{v}^- - 2c_s^- \boldsymbol{s}\cdot\boldsymbol{En} = \boldsymbol{s}\cdot\boldsymbol{v}^+, \quad \boldsymbol{t}\cdot\boldsymbol{v}^- - 2c_s^- \boldsymbol{t}\cdot\boldsymbol{En} = \boldsymbol{t}\cdot\boldsymbol{v}^+.$$

These boundary conditions are enforced weakly through the numerical flux for the c_s characteristics, which results in

$$(\mathfrak{F}\boldsymbol{q})^* = \mathfrak{F}^- \boldsymbol{q}^- + \frac{\boldsymbol{n}\cdot[\![\boldsymbol{S}]\!] + \rho^+ c_p^+ [\![\boldsymbol{v}]\!]}{\rho^+ c_p^+ + \rho^- c_p^-}\left(\begin{array}{c}\boldsymbol{n}\otimes\boldsymbol{n}\\\rho^- c_p^- \boldsymbol{n}\end{array}\right) - \frac{1}{\rho^- c_s^-}\left(\begin{array}{c}\mathrm{sym}(\boldsymbol{n}\otimes(\boldsymbol{n}\times(\boldsymbol{n}\times[\![\boldsymbol{S}]\!])))\\\rho^- c_s^- \boldsymbol{n}\times(\boldsymbol{n}\times[\![\boldsymbol{S}]\!])\end{array}\right).$$

Note that this is the same as the numerical flux for the elastic–elastic region when $\mu^+ = 0$. Following a similar argument for the acoustic–elastic interface we find that the numerical flux coincides with the one for the acoustic–acoustic interface with $\mu^+ \neq 0$.

3.4. Unified flux for the coupled elastic–acoustic wave equations

Combining the results obtained in this section we arrive at the following unified formulation of the upwind numerical flux:

$$\boldsymbol{n}\cdot((\mathfrak{F}\boldsymbol{q})^* - \mathfrak{F}^- \boldsymbol{q}^-) = k_0(\boldsymbol{n}\cdot[\![\boldsymbol{S}]\!] + \rho^+ c_p^+ [\![\boldsymbol{v}]\!])\left(\begin{array}{c}\boldsymbol{n}\otimes\boldsymbol{n}\\\rho^- c_p^- \boldsymbol{n}\end{array}\right) - k_1\left(\begin{array}{c}\mathrm{sym}(\boldsymbol{n}\otimes(\boldsymbol{n}\times(\boldsymbol{n}\times[\![\boldsymbol{S}]\!])))\\\rho^- c_s^- \boldsymbol{n}\times(\boldsymbol{n}\times[\![\boldsymbol{S}]\!])\end{array}\right) - k_1\rho^+ c_s^+\left(\begin{array}{c}\mathrm{sym}(\boldsymbol{n}\otimes(\boldsymbol{n}\times(\boldsymbol{n}\times[\boldsymbol{v}])))\\\rho^- c_s^- \boldsymbol{n}\times(\boldsymbol{n}\times[\boldsymbol{v}])\end{array}\right),$$

$$(22\mathrm{a})$$

where $[\boldsymbol{v}] := \boldsymbol{v}^- - \boldsymbol{v}^+$, $[\![\boldsymbol{v}]\!] := \boldsymbol{n}^-\cdot\boldsymbol{v}^- + \boldsymbol{n}^+\cdot\boldsymbol{v}^+$, and $[\![\boldsymbol{S}]\!] := \boldsymbol{S}^-\boldsymbol{n}^- + \boldsymbol{S}^+\boldsymbol{n}^+$. The coefficients k_0 and k_1 are given by

$$k_0 = \frac{1}{\rho^- c_p^- + \rho^+ c_p^+}, \quad k_1 = \frac{1}{\rho^- c_s^- + \rho^+ c_s^+}. \qquad (22\mathrm{b})$$

For elastic–elastic and elastic–acoustic interfaces (i.e., with an elastic medium on the inward side, $\mu^- \neq 0$), both coefficients k_0, k_1 are well defined. For acoustic–elastic and acoustic–acoustic interfaces (i.e., with an acoustic medium on the inward side, $\mu^- = 0$), we simply use

$$k_1 = 0. \qquad (22\mathrm{c})$$

3.5. Imposing boundary conditions through the flux

We use the upwind numerical flux developed above not only to model interaction across element interfaces, but also to impose the traction boundary conditions (4) in a weak sense. This is accomplished by introducing extended material parameters $(\rho^+, \mu^+, \lambda^+) := (\rho^-, \mu^-, \lambda^-)$ to be used in the computation of the numerical flux (22). We define $\boldsymbol{q}^+$ as the extension of the

solution to the exterior, choosing its values so that the characteristics entering the element realize the desired traction $\boldsymbol{t}_{\mathrm{bc}}$. This approach leads to the following modification in the strain variables:

$$\boldsymbol{q}^+ = \begin{pmatrix} \boldsymbol{E}^+ \\ \boldsymbol{v}^+ \end{pmatrix} = \begin{pmatrix} \boldsymbol{E}^- \\ \boldsymbol{v}^- \end{pmatrix} + \begin{pmatrix} \boldsymbol{E}^{\mathrm{mod}} \\ 0 \end{pmatrix},$$

with

$$\boldsymbol{E}^{\mathrm{mod}} = \left(\frac{2}{\lambda^- + 2\mu^-} - \frac{2}{\mu^-} \right)(\boldsymbol{n} \cdot (\boldsymbol{t}_{\mathrm{bc}} - \boldsymbol{S}^-\boldsymbol{n}))(\boldsymbol{n} \otimes \boldsymbol{n}) + \frac{2}{\mu^-}\mathrm{sym}(\boldsymbol{n} \otimes (\boldsymbol{t}_{\mathrm{bc}} - \boldsymbol{S}^-\boldsymbol{n}))$$

in the elastic regime and

$$\boldsymbol{E}^{\mathrm{mod}} = \frac{2}{\lambda^-}(\boldsymbol{n} \cdot (\boldsymbol{t}_{\mathrm{bc}} - \boldsymbol{S}^-\boldsymbol{n}))(\boldsymbol{n} \otimes \boldsymbol{n})$$

in the acoustic regime. We refer to [26] for a more detailed study of imposing different types of physical boundary conditions in two dimensions by means of characteristics.

It follows from a short computation that at domain boundaries

$$\boldsymbol{S}^+\boldsymbol{n} = (\boldsymbol{C}\boldsymbol{E}^+)\boldsymbol{n} = \begin{cases} 2\boldsymbol{t}_{\mathrm{bc}} - \boldsymbol{S}^-\boldsymbol{n} & \text{in the elastic regime,} \\ 2(\boldsymbol{n} \cdot \boldsymbol{t}_{\mathrm{bc}})\boldsymbol{n} - \boldsymbol{n} \times (\boldsymbol{n} \times (\boldsymbol{S}^-\boldsymbol{n})) - (\boldsymbol{n} \cdot \boldsymbol{S}^-\boldsymbol{n})\boldsymbol{n} & \text{in the acoustic regime.} \end{cases}$$

This implies for the jumps and differences across the boundary that

$$[\![\boldsymbol{v}]\!] = 0, \tag{23a}$$
$$[\boldsymbol{v}] = 0, \tag{23b}$$

$$[\![\boldsymbol{S}]\!] = \begin{cases} -2(\boldsymbol{t}_{\mathrm{bc}} - \boldsymbol{S}^-\boldsymbol{n}) & \text{in the elastic regime,} \\ -2\boldsymbol{n} \cdot (\boldsymbol{t}_{\mathrm{bc}} - \boldsymbol{S}^-\boldsymbol{n})\boldsymbol{n} & \text{in the acoustic regime.} \end{cases} \tag{23c}$$

Substituted into the numerical flux (22), this form of the jump terms illustrates the fact that the boundary condition enforces the traction on elastic boundaries while enforcing only the normal component of the traction on acoustic boundaries.

3.6. Corresponding velocity–stress dG method

We now show the close relation between the velocity–strain dG formulation (9) with numerical flux (22) and a first-order velocity–stress dG discretization. Using the definition of the inner product (8) and $\boldsymbol{q} = (\boldsymbol{E}, \boldsymbol{v})^T$ and $\boldsymbol{p} = (\boldsymbol{H}, \boldsymbol{w})^T$ in (9), we obtain

$$\int_{\mathrm{D}^e} \frac{\partial \boldsymbol{E}}{\partial t} : \boldsymbol{C}\boldsymbol{H}d\boldsymbol{x} + \int_{\mathrm{D}^e} \rho \frac{\partial \boldsymbol{v}}{\partial t} \cdot \boldsymbol{w}d\boldsymbol{x} - \int_{\mathrm{D}^e} \frac{1}{2}(\nabla \boldsymbol{v} + \nabla \boldsymbol{v}^T) : \boldsymbol{C}\boldsymbol{H}d\boldsymbol{x}$$
$$- \int_{\mathrm{D}^e} (\nabla \cdot (\boldsymbol{C}\boldsymbol{E})) \cdot \boldsymbol{w}d\boldsymbol{x} + \int_{\partial \mathrm{D}^e} \left(\boldsymbol{n} \cdot \left(\left(\mathfrak{F}\begin{pmatrix} \boldsymbol{E} \\ \boldsymbol{v} \end{pmatrix} \right)^* - \mathfrak{F}^-\begin{pmatrix} \boldsymbol{E}^- \\ \boldsymbol{v}^- \end{pmatrix} \right) \right) \cdot \begin{pmatrix} \boldsymbol{C}\boldsymbol{H}^- \\ \boldsymbol{w}^- \end{pmatrix}d\boldsymbol{x} = \int_{\mathrm{D}^e} \boldsymbol{f} \cdot \boldsymbol{w}d\boldsymbol{x}. \tag{24}$$

Using that the constitutive tensor $\boldsymbol{C}$ is symmetric and that $\boldsymbol{S} = \boldsymbol{C}\boldsymbol{E}$, (24) is equivalent to

$$\int_{\mathrm{D}^e} \frac{\partial \boldsymbol{S}}{\partial t} : \boldsymbol{H}d\boldsymbol{x} + \int_{\mathrm{D}^e} \rho \frac{\partial \boldsymbol{v}}{\partial t} \cdot \boldsymbol{w}d\boldsymbol{x} - \int_{\mathrm{D}^e} \frac{1}{2}\boldsymbol{C}(\nabla \boldsymbol{v} + \nabla \boldsymbol{v}^T) : \boldsymbol{H}d\boldsymbol{x}$$
$$- \int_{\mathrm{D}^e} (\nabla \cdot \boldsymbol{S}) \cdot \boldsymbol{w}d\boldsymbol{x} + \int_{\partial \mathrm{D}^e} \left(\boldsymbol{n} \cdot \left(\left(\widetilde{\mathfrak{F}}\begin{pmatrix} \boldsymbol{S} \\ \boldsymbol{v} \end{pmatrix} \right)^* - \widetilde{\mathfrak{F}}^-\begin{pmatrix} \boldsymbol{S}^- \\ \boldsymbol{v}^- \end{pmatrix} \right) \right) \cdot \begin{pmatrix} \boldsymbol{H}^- \\ \boldsymbol{w}^- \end{pmatrix}d\boldsymbol{x} = \int_{\mathrm{D}^e} \boldsymbol{f} \cdot \boldsymbol{w}d\boldsymbol{x}, \tag{25a}$$

where the numerical flux for this velocity–stress formulation is found by moving $\boldsymbol{C}$ to the left hand side in the boundary integral, which results in

$$\boldsymbol{n} \cdot \left(\left(\widetilde{\mathfrak{F}}\begin{pmatrix} \boldsymbol{S} \\ \boldsymbol{v} \end{pmatrix} \right)^* - \widetilde{\mathfrak{F}}^-\begin{pmatrix} \boldsymbol{S}^- \\ \boldsymbol{v}^- \end{pmatrix} \right) = k_0(\boldsymbol{n} \cdot [\![\boldsymbol{S}]\!] + \rho^+ c_p^+ [\![\boldsymbol{v}]\!]) \begin{pmatrix} \lambda^-\boldsymbol{I} + 2\mu^-\boldsymbol{n} \otimes \boldsymbol{n} \\ \rho^- c_p^-\boldsymbol{n} \end{pmatrix}$$
$$- k_1 \begin{pmatrix} 2\mu^-\mathrm{sym}(\boldsymbol{n} \otimes (\boldsymbol{n} \times (\boldsymbol{n} \times [\![\boldsymbol{S}]\!]))) \\ \rho^- c_s^-\boldsymbol{n} \times (\boldsymbol{n} \times [\![\boldsymbol{S}]\!]) \end{pmatrix}$$
$$- k_1 \rho^+ c_s^+ \begin{pmatrix} 2\mu^-\mathrm{sym}(\boldsymbol{n} \otimes (\boldsymbol{n} \times (\boldsymbol{n} \times [\boldsymbol{v}]))) \\ \rho^- c_s^-\boldsymbol{n} \times (\boldsymbol{n} \times [\boldsymbol{v}]) \end{pmatrix}. \tag{25b}$$

Consequently, the only difference between the dG methods based on the velocity–strain and the velocity–stress formulation is the choice of the unknowns for the computation. If the constitutive tensor $\boldsymbol{C}$ acts on the test function $\boldsymbol{H}$ for the strain component, the primary unknowns are velocity and strain; if $\boldsymbol{C}$ acts on $\boldsymbol{E}$, only the stress $\boldsymbol{S} = \boldsymbol{C}\boldsymbol{E}$ appears in the formulation, which allows one to choose stress and velocity as primary unknowns.

4. Consistency of flux and stability

At this point we have developed the discontinuous Galerkin formulation (9), including the specification of a numerical flux and boundary conditions, in an infinite- or finite-dimensional function space. Furthermore, the integrals have not yet been subjected to any numerical approximation, i.e., we assume exact integration. Under these conditions, we next show consistency of the numerical flux and stability of the dG method.

4.1. Consistency of the numerical flux

The numerical flux (22), which has been computed as the exact solution of a Riemann problem, uses material properties from both elements neighboring a face. Here we show that this choice leads to a consistent scheme.

Theorem 1. *The dG scheme (9) with the numerical flux (22) is a consistent numerical scheme.*

Proof. Substitution of the exact strain–velocity solution of the elastic–acoustic wave equations, denoted $\boldsymbol{q}_{\text{ex}}$, into (9), and making use of the interface conditions (5) and (6) in (22), results in

$$\boldsymbol{n} \cdot \left((\mathfrak{F}\boldsymbol{q}_{\text{ex}})^* - \mathfrak{F}^- \boldsymbol{q}_{\text{ex}}^- \right) = 0.$$

Thus consistency for all possible combinations of elastic and acoustic media holds. $\square$

In contrast, the numerical flux used in [19,24] (which is based on a velocity–stress formulation of the wave equation) uses only material parameters from the interior of the element for the numerical flux computation. This simplification can be problematic for the consistency of the scheme, in particular at acoustic–elastic interfaces.

If one takes in (22) material properties from one side of the interface only, say the negative side, then the resulting "one-sided" numerical flux, $(\mathfrak{F}\boldsymbol{q})^\dagger$, satisfies

$$\boldsymbol{n} \cdot \left((\mathfrak{F}\boldsymbol{q})^\dagger - \mathfrak{F}^- \boldsymbol{q}^- \right) = \frac{\boldsymbol{n} \cdot [\![\boldsymbol{S}]\!] + \rho^- c_p^- [\![\boldsymbol{v}]\!]}{2\rho^- c_p^-} \begin{pmatrix} \boldsymbol{n} \otimes \boldsymbol{n} \\ \rho^- c_p^- \boldsymbol{n} \end{pmatrix} - \frac{1}{2\rho^- c_s^-} \begin{pmatrix} \text{sym}(\boldsymbol{n} \otimes (\boldsymbol{n} \times (\boldsymbol{n} \times [\![\boldsymbol{S}]\!]))) \\ \rho^- c_s^- \boldsymbol{n} \times (\boldsymbol{n} \times [\![\boldsymbol{S}]\!]) \end{pmatrix} - \frac{1}{2} \begin{pmatrix} \text{sym}(\boldsymbol{n} \otimes (\boldsymbol{n} \times (\boldsymbol{n} \times [\boldsymbol{v}]))) \\ \rho^- c_s^- \boldsymbol{n} \times (\boldsymbol{n} \times [\boldsymbol{v}]) \end{pmatrix}.$$

Using condition (6) for an elastic–acoustic interface we obtain

$$\boldsymbol{n} \cdot \left((\mathfrak{F}\boldsymbol{q}_{\text{ex}})^\dagger - \mathfrak{F}^- \boldsymbol{q}_{\text{ex}}^- \right) = -\frac{1}{2} \begin{pmatrix} \text{sym}(\boldsymbol{n} \otimes (\boldsymbol{n} \times (\boldsymbol{n} \times [\boldsymbol{v}]))) \\ \rho^- c_s^- \boldsymbol{n} \times (\boldsymbol{n} \times [\boldsymbol{v}]) \end{pmatrix}.$$

This expression is generally nonzero since the tangential component of the velocity is not necessarily continuous at such an interface. Thus, this one-sided numerical flux is not consistent at interfaces involving an acoustic medium.

A similar inconsistency for elastic–acoustic interfaces exists in the numerical flux used for solving the coupled elastic–acoustic wave equations presented in [19]. To study this issue, we implemented the dG scheme (25), which is based on the velocity–stress formulation of the wave equation. We verified that the numerical results for the velocity are identical to those obtained from the velocity–strain formulation for constant material properties and element-wise constant Jacobian determinant (see the discussion in Section 3.6). In particular, when we tested this method on the elastic–acoustic interaction problem defined in Section 6.2, we observed convergence identical to Fig. 3(b) if parameters of the medium from both sides of the interface were used. Taking the material parameters from the negative side only, the flux (25b) reduces to the one used in [19]. For this one-sided form of the numerical flux, in which only the negative-side material parameters are used, the numerical solution did not converge to the exact solution in the L^2-norm as the mesh was refined or the polynomial order increased. Thus, we conclude that it is critical that the numerical flux take into account the neighboring material values at elastic–acoustic interfaces.

4.2. Stability

In this section we prove stability of the discontinuous Galerkin scheme (9) by studying the time evolution of an energy functional. While in the proof below we assume exact integration, we sketch the extension of the stability result to a common numerical quadrature scheme for conforming meshes in Section 5.5.

Theorem 2. *Let us consider an energy functional $\mathcal{E}(t)$ defined as follows,*

$$\mathcal{E}(t) := \sum_{e=1}^{N_{\text{el}}} \mathcal{E}^e(t) \quad \text{where } \mathcal{E}^e(t) := \frac{1}{2} \int_{\mathrm{D}^e} (\boldsymbol{E} : (\mathbf{C}\boldsymbol{E}) + \rho \boldsymbol{v} \cdot \boldsymbol{v}) d\boldsymbol{x}.$$

Let us also assume periodic or traction-free boundary conditions (i.e., $\boldsymbol{t}_{\text{bc}} = 0$). Then the dG discretization is stable in the sense that there exists a constant C such that

$$\frac{d}{dt}\mathcal{E} \leqslant C\Big(\mathcal{E} + \|\boldsymbol{f}\|_{L^2(\Omega)}\Big). \tag{26}$$

Moreover, if $\boldsymbol{f} = 0$, then $\frac{d}{dt}\mathcal{E} \leqslant 0$ and thus $\mathcal{E}$ is non-increasing.

Proof. Inserting $\boldsymbol{p} := \begin{pmatrix} \boldsymbol{S} \\ \boldsymbol{v} \end{pmatrix} = \begin{pmatrix} \boldsymbol{CE} \\ \boldsymbol{v} \end{pmatrix}$ into (9) yields

$$\int_{D^e}\Big(\frac{d\boldsymbol{E}}{dt} : \boldsymbol{S} + \rho\frac{d\boldsymbol{v}}{dt}\cdot\boldsymbol{v}\Big)d\boldsymbol{x} - \int_{D^e}\Big(\frac{1}{2}(\nabla\boldsymbol{v} + \nabla\boldsymbol{v}^T) : \boldsymbol{S} + (\nabla\cdot\boldsymbol{S})\cdot\boldsymbol{v}\Big)d\boldsymbol{x} + \int_{\partial D^e}(\boldsymbol{n}\cdot((\mathfrak{F}\boldsymbol{q})^* - \mathfrak{F}^-\boldsymbol{q}^-))\cdot\boldsymbol{p}d\boldsymbol{x} = \int_{D^e}\boldsymbol{f}\cdot\boldsymbol{v}d\boldsymbol{x}.$$

With the definition of $\mathcal{E}^e$ this implies

$$\frac{d}{dt}\mathcal{E}^e = \int_{D^e}\Big(\frac{1}{2}(\nabla\boldsymbol{v} + \nabla\boldsymbol{v}^T) : \boldsymbol{S} + (\nabla\cdot\boldsymbol{S})\cdot\boldsymbol{v}\Big)d\boldsymbol{x} - \int_{\partial D^e}(\boldsymbol{n}\cdot((\mathfrak{F}\boldsymbol{q})^* - \mathfrak{F}^-\boldsymbol{q}^-))\cdot\boldsymbol{p}d\boldsymbol{x} + \int_{D^e}\boldsymbol{f}\cdot\boldsymbol{v}d\boldsymbol{x}, \tag{27}$$

and after integration by parts in space,

$$\frac{d}{dt}\mathcal{E}^e = -\int_{D^e}\Big((\nabla\cdot\boldsymbol{S})\cdot\boldsymbol{v} + \frac{1}{2}(\nabla\boldsymbol{v} + \nabla\boldsymbol{v}^T) : \boldsymbol{S}\Big)d\boldsymbol{x} - \int_{\partial D^e}(\boldsymbol{n}\cdot(\mathfrak{F}\boldsymbol{q})^*)\cdot\boldsymbol{p}d\boldsymbol{x} + \int_{D^e}\boldsymbol{f}\cdot\boldsymbol{v}d\boldsymbol{x}. \tag{28}$$

Summing (27) and (28) and dividing by 2 yields

$$\frac{d}{dt}\mathcal{E}^e = -\int_{\partial D^e}(\boldsymbol{n}\cdot((\mathfrak{F}\boldsymbol{q})^* - \mathfrak{F}^-\boldsymbol{q}^-))\cdot\boldsymbol{p} + \frac{1}{2}(\boldsymbol{n}\cdot(\mathfrak{F}^-\boldsymbol{q}^-))\cdot\boldsymbol{p}d\boldsymbol{x} + \int_{D^e}\boldsymbol{f}\cdot\boldsymbol{v}d\boldsymbol{x}. \tag{29}$$

For the energy $\mathcal{E}$, it holds that

$$\frac{d}{dt}\mathcal{E} = \sum_{D^e}\frac{d}{dt}\mathcal{E}^e = \sum_{\substack{\text{faces } h \\ h = \partial D^e \cap \partial D^{e'}, e \neq e'}}\mathcal{E}_e^{e'} + \sum_{\substack{\text{faces } h \\ h = \partial D^e \cap \partial B}}\mathcal{E}_{\text{bc}}^e + \int_B\boldsymbol{f}\cdot\boldsymbol{v}d\boldsymbol{x}. \tag{30}$$

Here, $\mathcal{E}_e^{e'}$ denotes the contribution from the elements D^e and $D^{e'}$ to their shared face $\partial D^e \cap \partial D^{e'}$, and $\mathcal{E}_{\text{bc}}^e$ the contribution of stress-free element faces at the boundary. To compute $\mathcal{E}_e^{e'}$ we need to combine the element energy contribution from the elements D^e and $D^{e'}$ along their shared face. For this combination we choose a negative sign superscript to denote quantities, such as material properties and state variables, from element D^e, and a positive sign superscript to denote quantities from $D^{e'}$. The normal is selected such that $\boldsymbol{n} = \boldsymbol{n}^- = -\boldsymbol{n}^+$. A short computation shows that

$$\mathcal{E}_e^{e'} = \int_{\partial D^e} -k_0\Big((\boldsymbol{n}\cdot[\![\boldsymbol{S}]\!])^2 + \rho^- c_p^- \rho^+ c_p^+[\![\boldsymbol{v}]\!]^2\Big) - \big(\boldsymbol{n}\cdot\boldsymbol{v}^-(\boldsymbol{S}^-\boldsymbol{n})\cdot\boldsymbol{n} - \boldsymbol{n}\cdot\boldsymbol{v}^+(\boldsymbol{S}^+\boldsymbol{n})\cdot\boldsymbol{n}\big)$$
$$- k_1\big(-(\boldsymbol{n}\times(\boldsymbol{n}\times[\![\boldsymbol{S}]\!]))\cdot[\![\boldsymbol{S}]\!] - \rho^- c_s^- \rho^+ c_s^+(\boldsymbol{n}\times(\boldsymbol{n}\times[\![\boldsymbol{v}]\!]))\cdot[\![\boldsymbol{v}]\!]\big) + \big(\boldsymbol{n}\times(\boldsymbol{n}\times\boldsymbol{v}^-)\cdot(\boldsymbol{S}^-\boldsymbol{n}) - \boldsymbol{n}\times(\boldsymbol{n}\times\boldsymbol{v}^+)\cdot(\boldsymbol{S}^+\boldsymbol{n})\big)$$
$$+ \big((\boldsymbol{S}^-\boldsymbol{n})\cdot\boldsymbol{v}^- - (\boldsymbol{S}^+\boldsymbol{n})\cdot\boldsymbol{v}^+\big)d\boldsymbol{x}.$$

Note that for $(\boldsymbol{S}^-, \boldsymbol{v}^-)$,

$$-\boldsymbol{n}\cdot\boldsymbol{v}^-(\boldsymbol{S}^-\boldsymbol{n})\cdot\boldsymbol{n} + (\boldsymbol{n}\times(\boldsymbol{n}\times\boldsymbol{v}^-))\cdot(\boldsymbol{S}^-\boldsymbol{n}) = -(\boldsymbol{S}^-\boldsymbol{n})\cdot\boldsymbol{v}^-,$$

and analogously for $(\boldsymbol{S}^+, \boldsymbol{v}^+)$. Moreover, since for any vector a we have $-(\boldsymbol{n}\times(\boldsymbol{n}\times\boldsymbol{a}))\cdot\boldsymbol{a} = \|\boldsymbol{n}\times(\boldsymbol{n}\times\boldsymbol{a})\|^2$, it follows that

$$\mathcal{E}_e^{e'} = \int_{\partial D^e} -k_0\Big((\boldsymbol{n}\cdot[\![\boldsymbol{S}]\!])^2 + \rho^- c_p^- \rho^+ c_p^+[\![\boldsymbol{v}]\!]^2\Big) - k_1\Big(\|\boldsymbol{n}\times(\boldsymbol{n}\times[\![\boldsymbol{S}]\!])\|^2 + \rho^- c_s^- \rho^+ c_s^+\|\boldsymbol{n}\times(\boldsymbol{n}\times[\![\boldsymbol{v}]\!])\|^2\Big)d\boldsymbol{x} \leqslant 0. \tag{31}$$

Next, we consider the contributions $\mathcal{E}_{\text{bc}}^e$ of the boundary faces to $\frac{d}{dt}\mathcal{E}$. Recall from Section 3.5 that for an element on the domain boundary, $\rho^- = \rho^+ =: \rho$, $c_p^- = c_p^+ =: c_p$, and $c_s^- = c_s^+ =: c_s$. For a boundary face of an elastic element it follows from (23) and (29) that

$$\mathcal{E}_{\text{bc}}^e = -\frac{1}{\rho c_p}((\boldsymbol{S}^-\boldsymbol{n})\cdot\boldsymbol{n})\big((\boldsymbol{S}^-\boldsymbol{n})\cdot\boldsymbol{n} + \rho c_p\boldsymbol{v}^-\cdot\boldsymbol{n}\big) + \boldsymbol{v}^-\cdot(\boldsymbol{S}^-\boldsymbol{n}) + \frac{1}{\rho c_s}(\boldsymbol{n}\times(\boldsymbol{n}\times(\boldsymbol{S}^-\boldsymbol{n})))\cdot\boldsymbol{S}^-\boldsymbol{n} + (\boldsymbol{n}\times(\boldsymbol{n}\times(\boldsymbol{S}^-\boldsymbol{n})))\cdot\boldsymbol{v}^-$$
$$= -\frac{1}{\rho c_p}((\boldsymbol{S}^-\boldsymbol{n})\cdot\boldsymbol{n})^2 - \frac{1}{\rho c_s}\|\boldsymbol{n}\times(\boldsymbol{n}\times(\boldsymbol{S}^-\boldsymbol{n}))\|^2 \leqslant 0. \tag{32}$$

Similarly, for an acoustic medium we derive

$$\mathcal{E}_{\text{bc}}^e = -\frac{1}{\rho c_p}((\boldsymbol{S}^-\boldsymbol{n})\cdot\boldsymbol{n})^2 \leqslant 0.$$

Now, for $\boldsymbol{f} = 0$ we obtain from (30) with (31) and (32) that the overall energy is non-increasing, i.e.,

$$\frac{d}{dt}\mathcal{E} \leqslant 0.$$

For $\boldsymbol{f} \neq 0$ the stability estimate follows from

$$\frac{d}{dt}\mathcal{E} \leqslant \int_B \boldsymbol{f} \cdot \boldsymbol{v} \leqslant C_1\left(\|\boldsymbol{v}\|^2_{L^2(\Omega)} + \|\boldsymbol{f}\|^2_{L^2(\Omega)}\right) \leqslant C\left(\mathcal{E} + \|\boldsymbol{f}\|^2_{L^2(\Omega)}\right),$$

with constants C_1, C, where we used that $\rho \geqslant \rho_0 > 0$ for a constant ρ_0. This completes the proof. $\square$

Note that the estimates (31) and (32) in the above stability proof yield the amount of dissipation occurring at element faces. This dissipation is caused by the upwind numerical flux in our dG scheme. It is proportional to the jumps in tractions and velocities, which tend to zero as the dG approximation converges to the exact solution. Using a test problem on a periodic domain we show implicitly in Section 6.1 that, in particular for orders $N \geqslant 3$, the dissipation is small, allowing accurate time integration for over 50 wave lengths.

5. Spectral discontinuous Galerkin discretization

In this section we complete the description of the numerical discontinuous Galerkin scheme by introducing local discrete tensor-product approximation spaces over curvilinear elements that cover the domain. We also comment on constant-state preservation and on time integration.

5.1. Local approximation spaces

To introduce the discontinuous Galerkin spatial discretization, we recall that B is partitioned into N_{el} curvilinear elements such that $B \approx B^{N_{\mathrm{el}}} = \bigcup_{e=1}^{N_{\mathrm{el}}} \mathrm{D}^e$. For each element D^e we assume that there is a diffeomorphic mapping $\boldsymbol{X}^e$ such that $\boldsymbol{X}^e(\boldsymbol{r}) \in \mathrm{D}^e$ for all $\boldsymbol{r} \in \widehat{\mathrm{D}}$, where $\widehat{\mathrm{D}}$ is the reference element. The vertices, edges, and faces of D^e are then the images under $\boldsymbol{X}^e$ of the vertices, edges, and faces of $\widehat{\mathrm{D}}$, respectively. Let us now introduce the discontinuous Galerkin space

$$\boldsymbol{V}_N := \left\{\boldsymbol{q}_N \in L^2(B^{N_{\mathrm{el}}}) : \boldsymbol{q}_N|_{\mathrm{D}^e} \circ \boldsymbol{X}^e \in R_N(\widehat{\mathrm{D}})\right\},$$

where $R_N(\widehat{\mathrm{D}})$ is a local approximation space of order N on the reference element. Classical examples for approximation spaces on the reference element are P_N, the set of polynomials of order at most N, and Q_N, the tensor product of one-dimensional polynomials of at most order N. We define the semi-discrete solution $\boldsymbol{q}_N$ of the coupled elastic and acoustic wave equations as an element in $\boldsymbol{V}_N := V_{N,\mathrm{sym}}^{3\times3} \oplus V_N^3$ as follows: find $\boldsymbol{q}_N \in \boldsymbol{V}_N$ such that for all $\mathrm{D}^e \in B^{N_{\mathrm{el}}}$ we have

$$\int_{\mathrm{D}^e} \boldsymbol{Q}\frac{\partial \boldsymbol{q}_N}{\partial t} \cdot \boldsymbol{p}_N d\boldsymbol{x} + \int_{\mathrm{D}^e} (\nabla \cdot \mathfrak{F}\boldsymbol{q}_N) \cdot \boldsymbol{p}_N d\boldsymbol{x} + \int_{\partial \mathrm{D}^e} \left(\boldsymbol{n} \cdot \left((\mathfrak{F}\boldsymbol{q}_N)^* - \mathfrak{F}^-\boldsymbol{q}_N^-\right)\right) \cdot \boldsymbol{p}_N d\boldsymbol{x} = \int_{\mathrm{D}^e} \boldsymbol{g} \cdot \boldsymbol{p}_N d\boldsymbol{x} \quad \text{for all } \boldsymbol{p}_N \in \boldsymbol{V}_N, \tag{33}$$

where $\boldsymbol{n}$ is the outward normal at the boundary of element D^e, and $\boldsymbol{n} \cdot (\mathfrak{F}\boldsymbol{q}_N)^*$ is the numerical flux developed in Section 3 applied to $\boldsymbol{q}_N$.

5.2. Discontinuous spectral element discretization

The discontinuous spectral element method is a specialization of the dG method to nodal hexahedral elements, endowed with tensor-product polynomial approximation spaces, where numerical integration is based on the same nodes as the polynomial interpolation. An important property of this approach is that the discrete mass matrix is diagonal, which avoids the solution of linear systems of equations in explicit time integration. Additionally, the tensor-product structure of the approximation space allows for an efficient implementation of derivatives on the element level, see e.g., [27]. However, this approach results in under-integration (i.e., committing quadrature errors), which requires careful treatment of the numerical flux through non-conforming element faces to ensure discrete stability of the scheme.

We consider a hexahedral reference element $\widehat{\mathrm{D}} = [-1,1]^3$. On each element D^e the numerical solution $\boldsymbol{q}_N$ is specified as

$$\boldsymbol{q}_N|_{\mathrm{D}^e} \circ \boldsymbol{X}^e \in Q_{N,\mathrm{sym}}^{3\times3} \oplus Q_N^3, \quad \boldsymbol{X}^e : \widehat{\mathrm{D}} \rightarrow \mathrm{D}^e,$$

where $Q_N(\widehat{\mathrm{D}})$ is the space of polynomials of degree N in each variable r_i, $i = 1, 2, 3$, on the reference element.

We use a nodal basis for the numerical representation of these polynomials. Let $\{\xi_l\}$ and $\{\omega_l\}$ be the sets of Nth-degree Legendre–Gauss–Lobatto points and weights on $[-1,1]$, respectively, for $l \in \{0,1,\ldots,N\}$. Furthermore, let $\{\ell_l(\xi)\}$ be the Lagrange polynomials associated with the points $\{\xi_l\}$,

$$\ell_l(\xi) = \prod_{\substack{k=0,1,\ldots,N \\ k \neq l}} \frac{\xi - \xi_k}{\xi_l - \xi_k}.$$

The Lagrange interpolant of a function $h(\boldsymbol{r})$ on the reference element $\widehat{\mathrm{D}}$ is defined as

$$\mathcal{I}_N h(\boldsymbol{r}) = \sum_{l,m,n=0}^N h_{lmn}\ell_{lmn}(\boldsymbol{r}), \quad \boldsymbol{r} \in \widehat{\mathrm{D}},$$

where

$$h_{lmn} = h(\boldsymbol{\xi}_{lmn}), \quad \boldsymbol{\xi}_{lmn} = \begin{pmatrix} \xi_l \\ \xi_m \\ \xi_n \end{pmatrix} \in \widehat{\mathsf{D}}$$

and

$$\ell_{lmn}(\boldsymbol{r}) = \ell_l(r_1)\ell_m(r_2)\ell_n(r_3), \quad l, m, n \in \{0, 1, \ldots, N\}.$$

Integrals are approximated by Legendre–Gauss–Lobatto quadrature as follows,

$$\int_{\widehat{\mathsf{D}}} h(\boldsymbol{r}) d\boldsymbol{r} \approx \sum_{l,m,n=0,1,\ldots,N} \omega_l \omega_m \omega_n h_{lmn}. \tag{34}$$

This approximation is exact if the integrand is in the space $Q_{2N-1}(\widehat{\mathsf{D}})$.

The interpolation of prescribed element-wise functions in physical space, such as the material parameters or the source term $\boldsymbol{g}(\boldsymbol{x})$, may be written with a slight abuse of notation as

$$\mathcal{I}_N \boldsymbol{g}(\boldsymbol{x})|_{\mathsf{D}^e} = \sum_{l,m,n=0,1,\ldots,N} (\boldsymbol{g} \circ \boldsymbol{X}^e)(\boldsymbol{\xi}_{lmn})\ell_{lmn}\left((\boldsymbol{X}^e)^{-1}(\boldsymbol{x})\right).$$

The time-dependent numerical solution $\boldsymbol{q}_N(\boldsymbol{x}, t)$ on an element D^e is fully specified by the $(N+1)^3$ time-dependent coefficients $\boldsymbol{q}_{lmn}^e(t)$,

$$\boldsymbol{q}_N(\boldsymbol{x}, t)|_{\mathsf{D}^e} = \sum_{l,m,n=0,1,\ldots,N} \boldsymbol{q}_{lmn}^e(t)\ell_{lmn}\left((\boldsymbol{X}^e)^{-1}(\boldsymbol{x})\right).$$

5.3. Discrete constant-state preservation

A discontinuous Galerkin method is called constant-state preserving if a stationary solution, i.e., one where the flux is constant in space and no sources are present, does not change over time. While this property is easily proven in the continuous setting, the finite-dimensional spatial discretization can give rise to spurious source terms. We resolve this issue by choosing the invariant curl form of the metric identities in our numerical scheme. Let us thus begin by introducing some notation on geometric transformations. Following [23, Chapter 6], we identify the covariant basis vectors $\boldsymbol{a}_i^e$ of the mapping $\boldsymbol{X}^e$ as columns of the Jacobian matrix,

$$\boldsymbol{a}_i^e = \frac{\partial \boldsymbol{X}^e}{\partial r_i}, \quad i = 1, 2, 3.$$

The Jacobian determinant J^e may be written as

$$J^e = \left| \frac{\partial \boldsymbol{X}^e}{\partial \boldsymbol{r}} \right| = \boldsymbol{a}_i^e \cdot \left(\boldsymbol{a}_j^e \times \boldsymbol{a}_k^e \right), \quad i, j, k \text{ cyclic}.$$

Defining the contravariant vectors as $\boldsymbol{b}_i^e = \nabla r_i$ leads to the identities

$$J^e \boldsymbol{b}_i^e = \boldsymbol{a}_j^e \times \boldsymbol{a}_k^e, \quad i, j, k \text{ cyclic} \tag{35}$$

and

$$\sum_{i=1}^3 \frac{\partial (J^e \boldsymbol{b}_i^e)}{\partial r_i} = 0. \tag{36}$$

The connection to constant-state preservation is made by transforming the discontinuous Galerkin Eq. (9) to the reference element and inserting a spatially constant flux with zero source, which produces (36) as a necessary condition [22]. Furthermore, Eq. (36) is fundamental to the consistent discretization of adjoint equations, see, e.g., [28] for a related discussion.

When nonlinear geometric transformations are interpolated by polynomials, the derivative of the interpolant is generally different from the true derivative. In particular, the cross product form (35) exhibits this drawback and the discrete constant-state preservation

$$\sum_{i=1}^3 \frac{\partial \mathcal{I}_N (J^e \boldsymbol{b}_i^e)}{\partial r_i} = 0 \tag{37}$$

does not hold in general. The solution proposed in [22] is to use the invariant curl form

$$(J^e \boldsymbol{b}_i^e)_l = \frac{1}{2} \boldsymbol{e}_i \cdot \nabla_{\boldsymbol{r}} \times \left(\mathcal{I}_N (X_m^e \nabla_{\boldsymbol{r}} X_n^e - X_n^e \nabla_{\boldsymbol{r}} X_m^e) \right),$$
$$i = 1, 2, 3, \quad l, m, n = 1, 2, 3, \quad (l, m, n) \text{ cyclic}, \tag{38}$$

which satisfies (37). In particular, the use of the curl operator after the interpolation $\mathcal{I}_N$ yields a polynomial of at most degree $N - 1$, which is represented exactly by the basis functions $\ell_{lmn}(\boldsymbol{r})$.

Integrals across element faces require a normal vector and the area of the surface element. In the dG context we evaluate only the product of these two, which permits us to reuse $J^e\boldsymbol{b}_i^e$ as defined in (38) for the scaled normal pointing along the image under $\boldsymbol{X}^e$ of the reference coordinate direction r_i. We refer to the appropriate choice of direction for a given boundary face as $J^e\boldsymbol{b}^e$. Using identical polynomial representations for the geometry on both sides of each face, we ensure that points on element faces see identical normals for elements on either side (modulo sign).

We use non-conforming meshes as created by adaptive h-refinement, which leads to element interfaces with one parent face on one side and four child faces on the other. At these non-conforming interfaces we need to satisfy two requirements. First, we must ensure that the surface element $J^e\boldsymbol{b}^e$ is represented by identical polynomials on both sides of the possibly curved interface, which we do by aligning the geometry of the child face exactly with its parent face. Second, we use an L^2-projection when transferring information from child to parent faces [29], which renders numerical errors orthogonal to the approximation space. This step is essential for discrete stability since the fluxes on the faces are under-integrated by the tensor-product Legendre–Gauss–Lobatto quadrature (34).

5.4. Spectral discontinuous Galerkin scheme

Based on the definitions introduced previously, the discrete spectral discontinuous Galerkin method on the element D^e is transformed to the reference element as follows:

$$\int_{\hat{\mathrm{D}}} \mathcal{I}_N\left(\mathcal{I}_N(J^e)\mathcal{I}_N(\mathbf{Q})\frac{\partial \boldsymbol{q}_N}{\partial t}\right)\ell_{lmn}d\boldsymbol{r} + \int_{\hat{\mathrm{D}}} \sum_{i=1}^{3}\left(\frac{\partial}{\partial r_i}\mathcal{I}_N\left(J^e\boldsymbol{b}_i^e \cdot \mathcal{I}_N(\mathfrak{F}\boldsymbol{q}_N)\right)\right)\ell_{lmn}d\boldsymbol{r}$$

$$+ \int_{\partial\hat{\mathrm{D}}} \pi\mathcal{I}_N\left(J^e\boldsymbol{b}^e \cdot \left(\mathcal{I}_N((\mathfrak{F}\boldsymbol{q}_N)^*) - \mathcal{I}_N(\mathfrak{F}^-\boldsymbol{q}_N^-)\right)\right)\ell_{lmn}d\boldsymbol{r}$$

$$= \int_{\hat{\mathrm{D}}} \mathcal{I}_N(\mathcal{I}_N(J^e)\mathcal{I}_N(\boldsymbol{g}))\ell_{lmn}d\boldsymbol{r}, \quad l,m,n = 0,1,\ldots,N.$$

Here π is the L^2-projection operator onto non-conforming parent faces and the integrals are approximated by tensor-product Legendre–Gauss–Lobatto quadrature (34). Note that the inner product in (33) involves the $\mathbf{C}$ tensor in the product of the strains. In elastic media, $\mathbf{C}$ is invertible and can be removed in the above spectral dG scheme. In acoustic media, $\mathbf{C}$ eliminates the equations for off-diagonal elements in the strain tensor. Diagonal components are treated individually although only their sum is unique. To optimize the computation in acoustic media, the tensor $\mathbf{C}$ may be moved from the test to the ansatz functions, resulting in a single equation for the trace of the strain tensor.

5.5. Stability for the spatially fully discrete case

The stability proof in Section 4.2 assumes exact quadrature and does not specify a spatial discretization scheme. Provided the mesh is conforming, this stability result can be extended to the spatially fully discrete case following a result on the equivalence of the strong and the weak dG form for Legendre–Gauss–Lobatto quadrature on hexahedral elements [30]. Due to this result, equivalence between (27) and (28) also holds for the non-exact Legendre–Gauss–Lobatto quadrature. The remaining parts of the proof for Theorem 2 can be adjusted in a straightforward way to the spatially fully discrete conforming mesh case, such that (26) also holds for a spatially fully discrete version of the energy functional $\mathcal{E}$.

5.6. Discretization in time

We use a method-of-lines approach to discretize the coupled elastic–acoustic wave equations. In space we use the discontinuous spectral element method previously discussed to generate a continuous-in-time system of ordinary differential equations. We choose to discretize in time with a five-stage fourth-order low-storage Runge–Kutta method [31]. In principle, a variety of time-stepping methods may be used, although the choice of (explicit) method affects the Courant–Friedrichs–Lewy (CFL) constant, and thus the largest possible stable time step.

To select a time step Δt, we use the CFL condition

$$\Delta t < C_{\mathrm{CFL}}\frac{\Delta x}{c_p \max(1, N^2)},$$

where c_p is the maximum longitudinal wave speed over an element, Δx is the minimum size of the elements in the mesh, and C_{CFL} is the CFL number. Since we use meshes that are adapted to the local wavelength, the right-hand side in the CFL condition varies at most by 2 times a factor depending on the element aspect ratio and distortion. Thus, using a global time step size Δt does not lead to overly small time steps.

6. Numerical results

In this section we demonstrate the high-order convergence rate of our method using several classical interface problems for which a reference solution is known. For each problem we present a brief description, which should be sufficient to reproduce the numerical solution. We conclude with a scalability study of our implementation, assessing parallel efficiency of the solution of a simplified global seismic wave propagation problem on up to 224,220 cores. Unless stated otherwise, we use a CFL number of 0.4.

6.1. Plane wave problem

In this first problem we investigate the numerical error in the velocity as time increases. The geometry for this problem is the periodic cube $[0,1] \times [0,1] \times [0,1]$, discretized into $8 \times 8 \times 8$ elements. Longitudinal and transverse plane waves are propagated through an elastic medium with $\lambda = 2.2$, $\mu = 1.3$, and $\rho = 1.2$. The direction of propagation for both waves is $\boldsymbol{p} = (0,0,1)^T$. The direction of motion for the longitudinal transverse waves is, respectively, $\boldsymbol{d}_p = \boldsymbol{p}$ and $\boldsymbol{d}_s = (0,1,0)^T$. The same wavenumber $k = 2\pi$ is used for both waves. For a given position $\boldsymbol{x}$ and time t, the exact displacement solution is given by

$$\boldsymbol{u} = \boldsymbol{d}_p \cos\left[k(\boldsymbol{x}\cdot\boldsymbol{p} - c_p t)\right] + \boldsymbol{d}_s \cos\left[k(\boldsymbol{x}\cdot\boldsymbol{p} - c_s t)\right].$$

Differentiating in time yields the velocity solution

$$\boldsymbol{v} = kc_p\boldsymbol{d}_p \sin\left[k(\boldsymbol{x}\cdot\boldsymbol{p} - c_p t)\right] + kc_s\boldsymbol{d}_s \sin\left[k(\boldsymbol{x}\cdot\boldsymbol{p} - c_s t)\right].$$

The L^2-error between the exact and dG velocity is shown in Fig. 2. The CFL number used is 0.4 for $N = 1\ldots4$, 0.1 for $N = 5\ldots6$, and 0.01 for $N = 7\ldots8$. It is selected to be small enough so that the error shown in Fig. 2 is dominated by the spatial error and not the temporal error.

6.2. Snell's law for an elastic–acoustic interface

In this problem we study convergence rates of the proposed discontinuous Galerkin scheme for a pressure plane wave incident on an acoustic–elastic interface. The incident wave in the acoustic fluid is reflected as a pressure wave and transmitted as longitudinal and transverse waves in the elastic solid. The geometry is shown in Fig. 3(a). The displacement of the generated transverse wave lies in the (x_1x_3)-plane (a so-called vertically-polarized transverse wave). Motion in the x_2-direction is not excited (this would correspond to a horizontally polarized transverse wave).

The derivation of the solution for this geometry may be found in [32, Section 4.6]. Given the form of the incident displacement wave,

$$\boldsymbol{w}_{\text{ip}}(\boldsymbol{x}, t) = C_{\text{ip}}\boldsymbol{d}_{\text{ip}} \cos\left(k_{\text{p1}}\left[x_1 \sin(\alpha_{\text{ip}}) + x_3 \cos(\alpha_{\text{ip}}) - \omega t\right]\right),$$

the reflected displacement wave is

$$\boldsymbol{w}_{\text{rp}}(\boldsymbol{x}, t) = C_{\text{rp}}\boldsymbol{d}_{\text{rp}} \cos\left(k_{\text{p1}}\left[x_1 \sin(\alpha_{\text{rp}}) - x_3 \cos(\alpha_{\text{rp}}) - \omega t\right]\right).$$

The transmitted longitudinal displacement wave is

$$\boldsymbol{w}_{\text{tp}}(\boldsymbol{x}, t) = C_{\text{tp}}\boldsymbol{d}_{\text{tp}} \cos\left(k_{\text{p2}}\left[x_1 \sin(\alpha_{\text{tp}}) + x_3 \cos(\alpha_{\text{tp}}) - \omega t\right]\right),$$

and the transmitted transverse displacement wave

$$\boldsymbol{w}_{\text{ts}}(\boldsymbol{x}, t) = C_{\text{ts}}\boldsymbol{d}_{\text{ts}} \cos\left(k_{\text{s2}}[x_1 \sin(\alpha_{\text{ts}}) + x_3 \cos(\alpha_{\text{ts}}) - \omega t]\right).$$
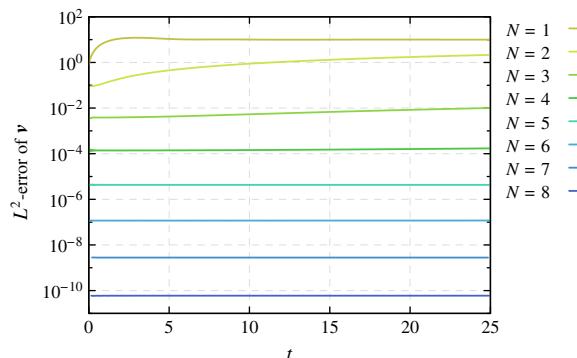

Fig. 2. Plane wave problem described in Section 6.1. Time evolution of the L^2-error in the velocity $\boldsymbol{v}$ for different orders of approximation N.
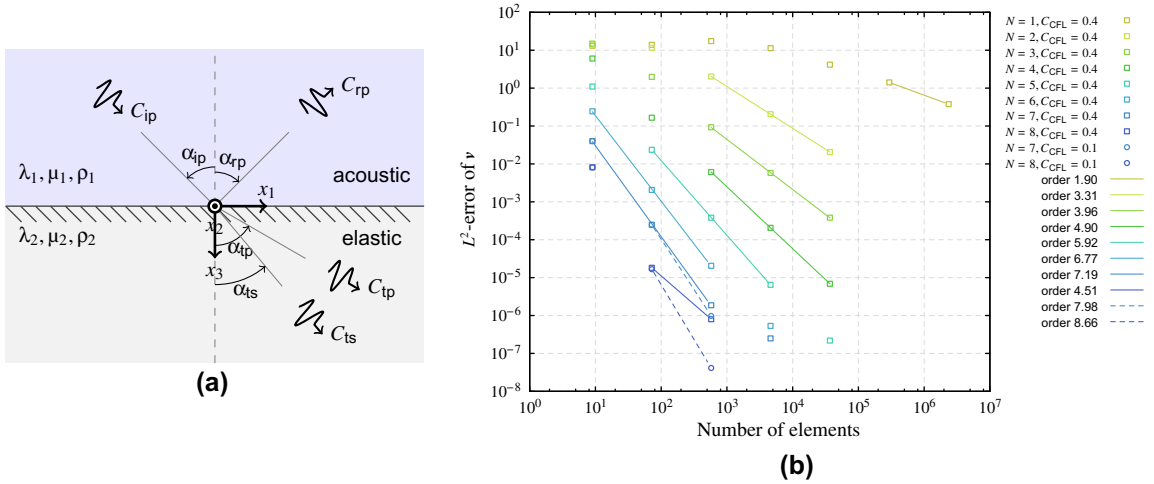
Fig. 3. Numerical solutions for Snell's Law problem described in Section 6.2. (a) Sketch of geometry featuring an incident pressure wave which reflects in the acoustic fluid as a pressure wave and transmits in the elastic solid as longitudinal and transverse waves. In this figure, C_{ip} is the magnitude of the pressure wave incident at angle α_{ip}, C_{rp} is the magnitude of the reflected pressure wave with emergent angle α_{rp}, C_{tp} is the magnitude of the transmitted longitudinal wave at angle α_{rp}, and C_{ts} the magnitude of the transmitted transverse wave at angle α_{rs}. Lamé parameters and density for the acoustic half-space are λ_1, μ_1, and ρ_1. For the elastic half-space the material parameters are λ_2, μ_2, and ρ_2. (b) Plot of the L^2-error in $\boldsymbol{v}$ at final time $t = 10$. The errors for specific mesh resolutions and approximation orders N are represented by squares. Least-squares fits of the errors for different approximation orders are plotted as lines whose slopes are reported in the key as the observed rates of convergence. Circles and dashed lines correspond to cases with a CFL constant reduced from 0.4 to 0.1.

Here, ω is the angular frequency; k_{p1}, k_{p2}, and k_{s2} are wavenumbers of the respective waves and α_{ip}, α_{rp}, α_{tp}, and α_{ts} are the associated propagation angles. The displacement directions are

$$\boldsymbol{d}_{ip} = \begin{pmatrix} \sin(\alpha_{ip}) \\ 0 \\ \cos(\alpha_{ip}) \end{pmatrix}, \quad \boldsymbol{d}_{rp} = \begin{pmatrix} \sin(\alpha_{rp}) \\ 0 \\ -\cos(\alpha_{rp}) \end{pmatrix}, \quad \boldsymbol{d}_{tp} = \begin{pmatrix} \sin(\alpha_{tp}) \\ 0 \\ \cos(\alpha_{tp}) \end{pmatrix}, \quad \boldsymbol{d}_{ts} = \begin{pmatrix} -\cos(\alpha_{ts}) \\ 0 \\ \sin(\alpha_{ts}) \end{pmatrix}.$$

For these waves the displacement may be written as

$$\boldsymbol{u}(\boldsymbol{x}, t) = \begin{cases} \boldsymbol{w}_{ip}(\boldsymbol{x}, t) + \boldsymbol{w}_{rp}(\boldsymbol{x}, t) & \text{if } x_3 < 0, \\ \boldsymbol{w}_{tp}(\boldsymbol{x}, t) + \boldsymbol{w}_{ts}(\boldsymbol{x}, t) & \text{otherwise.} \end{cases} \tag{39}$$

Given the wave speeds in each layer, $c_{p1} = \sqrt{(\lambda_1 + 2\mu_1)/\rho_1}$ (with $\mu_1 = 0$), $c_{p2} = \sqrt{(\lambda_2 + 2\mu_2)/\rho_2}$, and $c_{s2} = \sqrt{\mu_2/\rho_2}$, the wavenumbers are found from the angular frequency as follows:

$$k_{p1} = \frac{\omega}{c_{p1}}, \quad k_{p2} = \frac{\omega}{c_{p2}}, \quad k_{s2} = \frac{\omega}{c_{s2}}.$$

The propagation angles are related to the given incident angle α_{ip} through Snell's Law:

$$\frac{\sin \alpha_{ip}}{c_{p1}} = \frac{\sin \alpha_{rp}}{c_{p1}} = \frac{\sin \alpha_{tp}}{c_{p2}} = \frac{\sin \alpha_{ts}}{c_{s2}}.$$

Setting $x_3 = 0$ and substituting (39) into the elastic–acoustic boundary conditions (6) yields a system of equations that is solved for the amplitudes of the reflected and transmitted waves given the incident wave amplitude. These amplitudes are

$$C_{rp} = C_{ip} \frac{Z_{p2}(\cos(2\alpha_{ts}))^2 + Z_{s2}(\sin(2\alpha_{ts}))^2 - Z_{p1}}{Z_{p2}(\cos(2\alpha_{ts}))^2 + Z_{s2}(\sin(2\alpha_{ts}))^2 + Z_{p1}},$$

$$C_{tp} = C_{ip} \frac{c_{p1}\rho_1}{c_{p2}\rho_2} \frac{2Z_{p2}\cos(2\alpha_{ts})}{Z_{p2}(\cos(2\alpha_{ts}))^2 + Z_{s2}(\sin(2\alpha_{ts}))^2 + Z_{p1}},$$

$$C_{ts} = C_{ip} \frac{c_{p1}\rho_1}{c_{s2}\rho_2} \frac{2Z_{s2}\sin(2\alpha_{ts})}{Z_{p2}(\cos(2\alpha_{ts}))^2 + Z_{s2}(\sin(2\alpha_{ts}))^2 + Z_{p1}},$$

where

$$Z_{p1} = \frac{\rho_1 c_{p1}}{\cos \alpha_{ip}}, \quad Z_{p2} = \frac{\rho_2 c_{p2}}{\cos \alpha_{tp}}, \quad Z_{s2} = \frac{\rho_2 c_{s2}}{\cos \alpha_{ts}}.$$

We compute solutions using the proposed dG method for the specific case of $c_{p1} = 1$, $\rho_1 = 1$, $c_{p2} = 3$, $c_{s2} = 2$, $\rho_2 = 1$, $\omega = 2\pi$, $\alpha_{ip} = 0.2$, and $C_{ip} = 1.0$. The computational mesh is constructed to match the wavelength of the numerical solution by providing uniform points-per-wavelength for the smallest wavelength in each region. The acoustic region thus receives one level of mesh refinement beyond that of the elastic region, which creates a mesh that is non-conforming at the elastic–acoustic interface. The computational domain is $[-1,1] \times [-1,1] \times [-2,2]$ and the exact solution is prescribed by tractions on the boundary. The velocity error in the L^2-norm at the final time $t = 10$ is given in Fig. 3(b).

Observed convergence rates for this problem are higher than the expected rate $N + \frac{1}{2}$. Also apparent in the figure is the decrease in order of accuracy for $N = 7, 8$ for a CFL number of 0.4, caused by a dominating error associated with time discretization by the fourth-order Runge–Kutta method we use. Reducing the CFL constant to 0.1 is sufficient to suppress this error and re-expose the high-order spatial convergence rate. Alternatively, one could employ a higher-order Runge–Kutta method with the larger time step.

6.3. Rayleigh wave

Rayleigh waves are surface waves that travel along a free surface of a homogeneous isotropic elastic solid. These waves decay exponentially away from the surface and travel at a speed c_r that is lower than both the transverse wave speed c_s and the longitudinal wave speed c_p. We consider the half-space $x_3 < 0$ with a traction-free surface at $x_3 = 0$; the geometry is sketched in Fig. 4(a). This problem serves to verify our implementation and the accuracy of the traction-free boundary condition. A similar problem was solved numerically in [26].

As found in [33] the displacement of a Rayleigh wave can be expressed as

$$u_1(\boldsymbol{x}, t) = \left[A_1 e^{b_1 x_3} + A_2 e^{b_2 x_3}\right] \cos\left(k(x_1 - c_r t)\right),$$
$$u_2(\boldsymbol{x}, t) = 0,$$
$$u_3(\boldsymbol{x}, t) = \left[\frac{b_1}{k} A_1 e^{b_1 x_3} + \frac{k}{b_2} A_2 e^{b_2 x_3}\right] \sin\left(k(x_1 - c_r t)\right),$$

where

$$b_1 = k\left(1 - \frac{c_r^2}{c_p^2}\right)^{\frac{1}{2}}, \quad b_2 = k\left(1 - \frac{c_r^2}{c_s^2}\right)^{\frac{1}{2}}.$$

Note that the positive square root is taken for b_1 and b_2 since the solution must decay exponentially away from the traction-free surface. The coefficients A_1 and A_2 are not uniquely determined but instead satisfy

$$\left(2 - \frac{c_r^2}{c_s^2}\right) A_1 + 2 A_2 = 0.$$

The speed of the Rayleigh wave c_r satisfies the relation

$$\left(2 - \frac{c_r^2}{c_s^2}\right)^2 - 4\left(1 - \frac{c_r^2}{c_p^2}\right)^{\frac{1}{2}} \left(1 - \frac{c_r^2}{c_s^2}\right)^{\frac{1}{2}} = 0.$$

An explicit derivation of the Rayleigh wave speed may be found in [34].

We choose the material parameters $\lambda = \mu = \rho = 1$ and the wavenumber $k = 2\pi$. The computational domain is $[-1,1] \times [-1,1] \times [-20,0]$ with periodic boundary conditions in the x_1- and x_2-directions. As in [26] we use a traction-free boundary condition for $x_3 = 0$ and $x_3 = -20$. The traction-free boundary condition at $x_3 = -20$ is justified since the solution
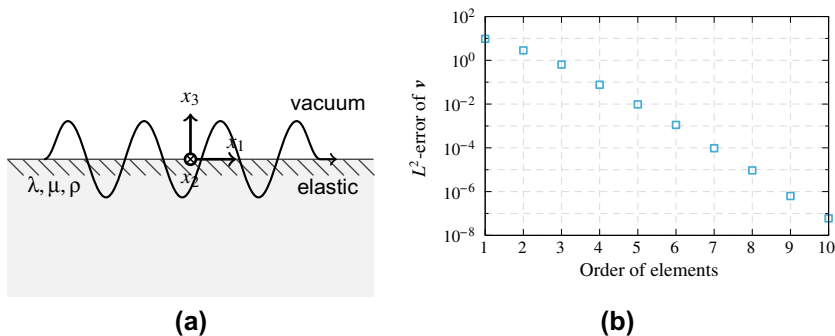

Fig. 4. Rayleigh wave problem described in Section (a). Sketch of the geometry. (b) Plot of the L^2-error of $\boldsymbol{v}$ at the time $t = 1$ for a Rayleigh wave traveling along the free surface.

decays exponentially away from $x_3 = 0$ and is of negligible magnitude at $x_3 = -20$. The domain is resolved by a uniform mesh consisting of $4 \times 4 \times 40$ elements. Fig. 4(b) shows exponential convergence of the numerical solution at time $t = 1$.

6.4. Lamb wave

Lamb waves propagate in an infinite elastic plate within a vacuum, where the direction of displacement lies in the plane spanned by the direction of motion, say the x_1-axis, and the direction of finite thickness $2d$ along the x_2-axis. There are two infinite families of solutions classified as symmetric and antisymmetric modes [33]. Here we solve for one of the symmetric modes and compare against the exact solution.

The displacement for a symmetric mode may be written as

$$u_1 = (-kB_1 \cos(px_2) - qB_2 \cos(qx_2)) \sin(kx_1 - \omega t),$$
$$u_2 = (-pB_1 \sin(px_2) + kB_2 \sin(qx_2)) \cos(kx_1 - \omega t),$$

where p and q are given by

$$p^2 = \frac{\omega^2}{c_p^2} - k^2, \quad q^2 = \frac{\omega^2}{c_s^2} - k^2.$$

To satisfy the traction-free boundary conditions, ω is related to the wavenumber k through

$$\frac{\tan(qd)}{\tan(pd)} = -\frac{4k^2 pq}{(q^2 - k^2)^2}.$$

The amplitudes B_1 and B_2 are not unique; their quotient must satisfy

$$\frac{B_1}{B_2} = \frac{2\mu kq \cos(qd)}{\left(\lambda k^2 + (\lambda + 2\mu)p^2\right) \cos(pd)}.$$

This problem, from [26], constitutes yet another test of the traction-free boundary condition. We use $d = 0.5$ and a uniform computational mesh consisting of $8 \times 4 \times 4$ elements covering the domain $[-1, 1] \times [-0.5, 0.5] \times [-0.5, 0.5]$, with periodic boundary conditions in the x_1- and x_3-directions. The elastic material parameters used are $\lambda = 2$, $\mu = 1$, and $\rho = 1$. The particular mode we solve for is characterized by $\omega = 13.13706319723$, $k = 2\pi$, $A = 126.1992721468$, and $B = 53.88807700007$. For element order 10, the CFL constant is set to 0.1 to lower the time error below the spatial error. Exponential convergence, for increasing approximation order, of the dG solution to the exact solution at time $t = 1$ is demonstrated in Fig. 5(b).

6.5. Scholte wave

Scholte waves are boundary waves that propagate along elastic–acoustic interfaces. Like Rayleigh waves, they decay exponentially away from the interface. This problem is designed to test the numerical flux between an acoustic medium and an elastic medium. We consider two half-spaces, as shown in Fig. 6(a). The upper half, $x_3 > 0$, is occupied by an acoustic medium with material parameters λ_1, $\mu_1 = 0$, and ρ_1. The lower half, $x_3 < 0$, contains an elastic medium with material parameters λ_2, μ_2, and ρ_2.

The displacement of a Scholte wave, which may be found in for example [32, Section 5.2], can be written for a given ω as
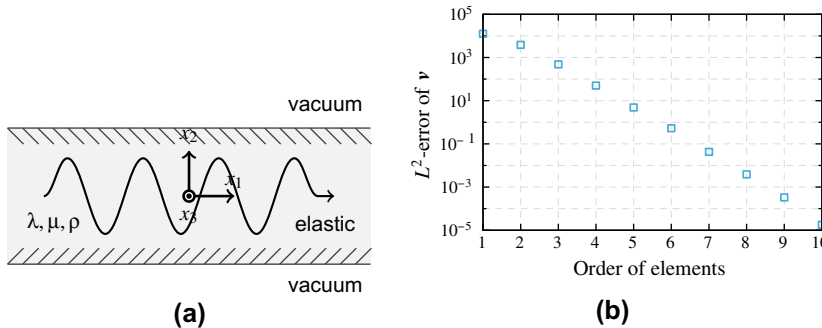

Fig. 5. Lamb wave problem described in Section 6.4. (a) Sketch of the geometry. (b) Plot of the L^2-error of $\mathbf{v}$ at time $t = 1$ for a Lamb wave traveling in an elastic plate.
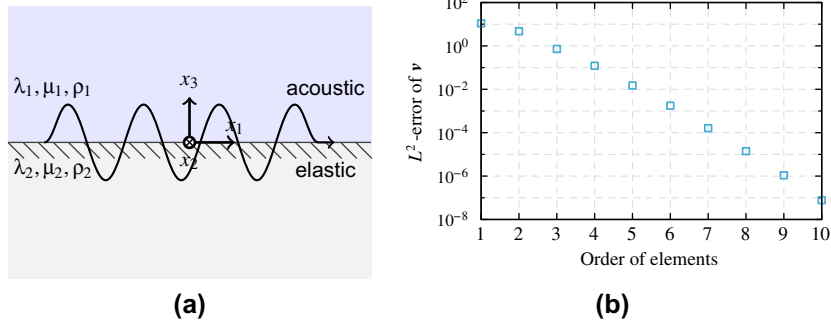
Fig. 6. Scholte wave problem described in Section 6.5. (a) Sketch of the geometry. (b) Plot of the L^2-error of $\mathbf{v}$ at time $t = 1$ for a Scholte wave traveling along an elastic–acoustic interface.

$$u_1 = \mathrm{Re}\left(ikB_1 e^{-kb_{1p}x_3} e^{i(kx_1-\omega t)}\right),$$
$$u_2 = 0,$$
$$u_3 = \mathrm{Re}\left(-kb_{1p}B_1 e^{-kb_{1p}x_3} e^{i(kx_1-\omega t)}\right)$$

for the acoustic region $x_3 > 0$ and

$$u_1 = \mathrm{Re}\left(\left(ikB_2 e^{kb_{2p}x_3} - kb_{2s}B_3 e^{kb_{2s}x_3}\right)e^{i(kx_1-\omega t)}\right),$$
$$u_2 = 0,$$
$$u_3 = \mathrm{Re}\left(\left(kb_{2p}B_2 e^{kb_{2p}x_3} + ikB_3 e^{kb_{2s}x_3}\right)e^{i(kx_1-\omega t)}\right),$$

for the elastic region $x_3 < 0$. The wavenumber is $k = \frac{\omega}{c}$, with decay rates

$$b_{1p} = \left(1 - \frac{c^2}{c_{1p}^2}\right)^{\frac{1}{2}}, \quad b_{2p} = \left(1 - \frac{c^2}{c_{2p}^2}\right)^{\frac{1}{2}}, \quad b_{2s} = \left(1 - \frac{c^2}{c_{2s}^2}\right)^{\frac{1}{2}},$$

where c is the Scholte wave speed. The longitudinal and transverse wave speeds in the two regions are

$$c_{1p} = \sqrt{\frac{\lambda_1 + 2\mu_1}{\rho_1}}, \quad c_{2p} = \sqrt{\frac{\lambda_2 + 2\mu_2}{\rho_2}}, \quad c_{2s} = \sqrt{\frac{\mu_2}{\rho_2}}.$$

Wave amplitudes can be related to each other by satisfying the interface condition (6) such that

$$2i\left(1 - \frac{c^2}{c_{2p}^2}\right)^{\frac{1}{2}}B_2 - \left(2 - \frac{c^2}{c_{2s}^2}\right)B_3 = 0, \tag{40a}$$

$$\frac{c^2}{c_{2s}^2}B_1 + \frac{\rho_2}{\rho_1}\left(2 - \frac{c^2}{c_{2s}^2}\right)B_2 + 2i\frac{\rho_2}{\rho_1}\left(1 - \frac{c^2}{c_{2s}^2}\right)^{\frac{1}{2}}B_3 = 0, \tag{40b}$$

$$\left(1 - \frac{c^2}{c_{1p}^2}\right)^{\frac{1}{2}}B_1 + \left(1 - \frac{c^2}{c_{2p}^2}\right)^{\frac{1}{2}}B_2 + iB_3 = 0. \tag{40c}$$

To ensure a nontrivial solution, the wave speed c is chosen such that the determinant of (40) is zero, which implies that c satisfies

$$\left(\frac{\rho_1}{\rho_2}b_{2p} + b_{1p}\right)r^4 - 4b_{1p}r^2 - 4b_{1p}(b_{2p}b_{2s} - 1) = 0,$$

where $r = \frac{c}{c_{2s}}$. It can be shown that a Scholte wave speed exists for arbitrary combinations of material parameters.

We use a uniform mesh consisting of $4 \times 4 \times 80$ elements covering the domain $[-1,1] \times [-1,1] \times [-20,20]$ with periodic boundary conditions in the x_1- and x_2-directions. The traction of the exact solution is imposed as a boundary condition at $x_3 = -20, 20$. The acoustic and elastic material parameters are $\lambda_1 = 1$, $\rho_1 = 1$, $\mu_1 = 0$, and $\lambda_2 = \mu_2 = 1$, $\rho_2 = 1$. For these material parameters, we obtain $c = 0.7110017230197$ and choose $B_1 = -i0.3594499773037$, $B_2 = -i0.8194642725978$, and $B_3 = 1$. Exponential convergence of the solution at time $t = 1$ can be inferred from Fig. 6(b).

6.6. Stoneley wave

Stoneley waves are boundary waves that propagate along elastic–elastic interfaces. As with Scholte and Rayleigh waves, Stoneley waves decay exponentially away from the interface. This problem tests the numerical flux between two elastic media. We consider two elastic half-spaces, depicted in Fig. 7(a). The upper half of the domain, $x_3 > 0$, is characterized by material parameters λ_1, μ_1 and ρ_1, while the lower half, $x_3 < 0$, is characterized by λ_2, μ_2 and ρ_2.

The displacement of the Stoneley wave, which may be found for example in [32, Section 5.2], can be written for a given ω as

$$u_1 = \mathrm{Re}\left(\left(ikB_1 e^{-kb_{2p}x_3} + kb_{2s}B_2 e^{-kb_{2s}x_3}\right)e^{i(kx_1-\omega t)}\right),$$
$$u_2 = 0,$$
$$u_3 = \mathrm{Re}\left(\left(-kb_{2p}B_1 e^{-kb_{2p}x_3} + ikB_2 e^{-kb_{2s}x_3}\right)e^{i(kx_1-\omega t)}\right)$$

for the upper half-space $x_3 > 0$ and

$$u_1 = \mathrm{Re}\left(\left(ikB_3 e^{kb_{2p}x_3} - kb_{2s}B_4 e^{kb_{2s}x_3}\right)e^{i(kx_1-\omega t)}\right),$$
$$u_2 = 0,$$
$$u_3 = \mathrm{Re}\left(\left(kb_{2p}B_3 e^{kb_{2p}x_3} + ikB_4 e^{kb_{2s}x_3}\right)e^{i(kx_1-\omega t)}\right)$$

for the lower half-space $x_3 < 0$. Here the wavenumber is $k = \frac{\omega}{c}$, with the decay rates

$$b_{1p} = \left(1 - \frac{c^2}{c_{1p}^2}\right)^{\frac{1}{2}}, \quad b_{1s} = \left(1 - \frac{c^2}{c_{1s}^2}\right)^{\frac{1}{2}}, \quad b_{2p} = \left(1 - \frac{c^2}{c_{2p}^2}\right)^{\frac{1}{2}}, \quad b_{2s} = \left(1 - \frac{c^2}{c_{2s}^2}\right)^{\frac{1}{2}},$$

where c is the Stoneley wave speed and the longitudinal and transverse wave speeds in the different regions are

$$c_{1p} = \sqrt{\frac{\lambda_1 + 2\mu_1}{\rho_1}}, \quad c_{1s} = \sqrt{\frac{\mu_1}{\rho_1}}, \quad c_{2p} = \sqrt{\frac{\lambda_2 + 2\mu_2}{\rho_2}}, \quad c_{2s} = \sqrt{\frac{\mu_2}{\rho_2}}.$$

The wave amplitudes can be related to each other through the interface condition (5) such that

$$\begin{pmatrix} b_{1p} & b_{2p} & -i & i \\ i & -i & b_{1s} & b_{2s} \\ -i2\mu_1 b_{1p} & -i2\mu_2 b_{2p} & -\mu_1(1+b_{1s}^2) & \mu_2(1+b_{2s}^2) \\ -\frac{\lambda_1 c^2}{c_{1p}^2} + 2\mu_1 b_{1p}^2 & \frac{\lambda_2 c^2}{c_{2p}^2} + 2\mu_2 b_{2p}^2 & -i2\mu_1 b_{1s} & -i2\mu_2 b_{2s} \end{pmatrix} \begin{pmatrix} B_1 \\ B_3 \\ B_2 \\ B_4 \end{pmatrix} = \begin{pmatrix} 0 \\ 0 \\ 0 \\ 0 \end{pmatrix}. \tag{41}$$

A nontrivial solution for the system (41) exists if its determinant vanishes, which amounts to finding a c such that the following equation is satisfied:

$$r^4\left(\left(\frac{\rho_1}{\rho_2}-1\right)^2 - \left(\frac{\rho_1}{\rho_2}b_{2p} + b_{1p}\right)\left(\frac{\rho_1}{\rho_2}b_{2s} + b_{1s}\right)\right) + 4r^2\left(\frac{\rho_1 c_{1s}^2}{\rho_2 c_{2s}^2}-1\right)\left(\frac{\rho_1}{\rho_2}b_{2p}b_{2s} - b_{1p}b_{1s} - \frac{\rho_1}{\rho_2}+1\right)$$
$$+ 4\left(\frac{\rho_1 c_{1s}^2}{\rho_2 c_{2s}^2}-1\right)^2 (b_{1p}b_{1s}-1)(b_{2p}b_{2s}-1) = 0,$$

with $r = \frac{c}{c_{2s}}$. A Stoneley wave exists only if the two transverse wave speeds are close to each other.

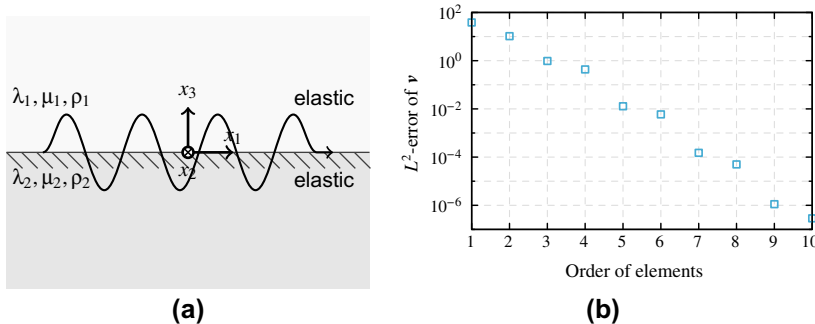**Fig. 7.** Stoneley wave problem described in Section 6.6. (a) Sketch of the geometry. (b) Plot of the L^2-error of $\boldsymbol{v}$ for a Stoneley wave traveling along an elastic–elastic interface at time $t = 1$.

For our numerical verification we use a uniform mesh of $4 \times 4 \times 80$ elements covering the domain $[-1,1] \times [-1,1] \times [-20,20]$ with periodic boundary conditions in the x_1- and x_2-directions. The traction of the exact solution is imposed as a boundary condition at $x_3 = -20, 20$. The elastic material parameters are $\lambda_1 = \mu_1 = 3$, $\rho_1 = 10$, and $\lambda_2 = \mu_2 = 1$, $\rho_2 = 1$. For these material parameters, it follows that $c = 0.5469813242138$, and we choose $B_1 = -i0.2952173626624$, $B_2 = -0.6798795208473$, $B_3 = i0.5220044931212$, and $B_4 = -0.9339639688697$. Exponential convergence is apparent from Fig. 7(b).

6.7. Seismic point source in an earth model

We have implemented a parallel version of the dG method presented in the previous sections and tested its scalability to a number of processor cores representative of the largest contemporary supercomputers. A description of the parallel algorithms and implementations underlying the code is beyond the scope of this article; see [35] for details on the algorithms underlying parallel mesh adaptation, and [36,37] for implementation and algorithmic issues underlying our framework for parallel h-adaptive discontinuous Galerkin methods. In this section we provide preliminary results on the scalability of a parallel implementation of our elastic–acoustic wave propagation code for a model problem in global seismology (a more detailed study is forthcoming). We consider a spherical domain with radially varying wave speeds taken from a simplified version of the Preliminary Reference Earth Model (PREM) [38]. The simplified model includes three concentric spherical shell regions: an elastic inner core, an acoustic outer core, and an elastic mantle. In each region, density and wave speeds are prescribed by third-degree polynomials depending on the radius. A curvilinear mesh is generated in parallel by the p4est library [35] in such a way that element boundaries conform to the spherical interfaces between these regions, across which the material properties are discontinuous. To ensure that the aspect ratio of the elements is uniformly close to unity throughout the mesh, the mesh is graded radially.

We simulate waves that originate from a seismic point source of a given maximal cutoff frequency. This frequency, along with the local wave velocity, determines the local wavelength. We use h-adaptive refinement of the mesh to tailor the ele-

(a) (b)

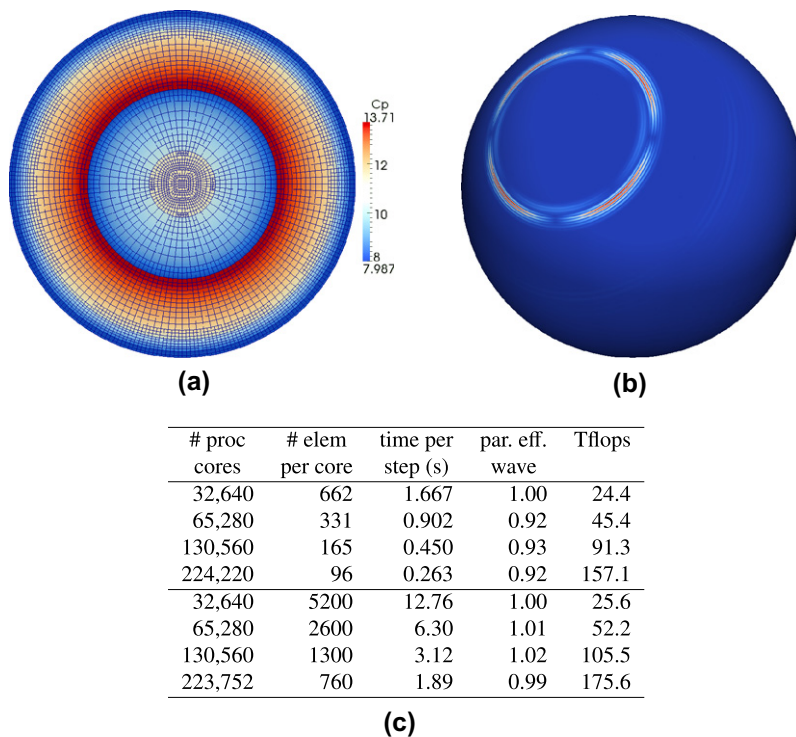| # proc cores	# elem per core	time per step (s)	par. eff. wave	Tflops
32,640	662	1.667	1.00	24.4
65,280	331	0.902	0.92	45.4
130,560	165	0.450	0.93	91.3
224,220	96	0.263	0.92	157.1
32,640	5200	12.76	1.00	25.6
65,280	2600	6.30	1.01	52.2
130,560	1300	3.12	1.02	105.5
223,752	760	1.89	0.99	175.6

(c)

Fig. 8. Simulation of global seismic wave propagation for a simplified PREM model. (a) Section through mesh that is adapted to the local wave speeds (low frequency source used for illustration purposes). (b) Snapshot from a wave propagation simulation with maximum resolved frequency of 0.1 Hz, degree $N = 4$, on 256 cores. (c) Strong scaling of global seismic wave propagation for a medium size problem (upper table, source frequency of 0.14 Hz) and a large problem (lower table, source frequency of 0.28 Hz) on up to 224 K cores of the (*Jaguar*) Cray XT5 at Oak Ridge National Laboratory. Degree $N = 6$ elements with at least 10 points per wavelength. Mesh for the medium size problem consists of 21.6 million elements, corresponding to 7.43 billion unknowns. Mesh for large problem consists of 170 million elements, corresponding to 53 billion unknowns. Here, the columns refers to the number of cores, the number of elements per core, the time taken per time step (based on an average of at least 100 time steps), the parallel efficiency of wave propagation (given by the ratio of measured to ideal speedup when solving the problem on an increasing number of cores for fixed problem size), and the sustained double precision floating point rate in teraflops/s (based on performance counters from the *PAPI* library [41]).

ment size to the shortest local wavelength (using c_s for elastic and c_p for acoustic media). Fig. 8(b) depicts a typical resulting h-non-conforming mesh. The required number of degrees of freedom scales with the third power of the frequency, and the time step size decreases linearly with increasing frequency, so that simulating high frequency seismic wave propagation in large regions quickly requires supercomputing resources (e.g., [39]). The earthquake point source is implemented via a moment tensor (e.g., [40]) and mollified by a Gaussian in space. Fig. 8(b) depicts a snapshot of the velocity magnitude for a maximum resolved frequency of 0.1 Hz. Fig. 8(c) presents results of a strong scalability study on a Cray XT5 supercomputer for a medium size problem (upper table, resolving up to 0.14 Hz) and a large problem (lower table, resolving up 0.28 Hz). In both cases, the problem size is kept fixed (at 7.43 billion and 53 billion unknowns, respectively) while the number of processor cores is increased to the full system size. Observed parallel efficiencies for three core doubling are in the 90–100% range. While these scalability results are preliminary, and the timings may be biased by system artifacts, they do suggest that high parallel efficiency is achievable for strong scalings out to the full numbers of cores on contemporary supercomputers.

7. Conclusions

The discontinuous Galerkin method presented in this article is based on a velocity–strain formulation, which allows the solution of the coupled elastic–acoustic wave equations in a unified framework and with high order accuracy. We give an explicit and simple-to-implement form of the numerical flux, which is computed as the exact solution of the relevant Riemann problem. Consistency of this flux and stability of the method in the presence of material discontinuities, including elastic–acoustic interfaces and free surfaces, are shown. Using exact solutions for interface problems such as Snell's Law and Rayleigh, Lamb, Scholte, and Stoneley wave problems, we show that the proposed method exhibits exponential convergence as the polynomial order of the elements increases. The high accuracy and low dispersion, the ability to accommodate h-non-conforming meshes resulting from h-adaptivity, and the parallel scalability to large numbers of cores make the method attractive for many wave propagation problems involving elastic–acoustic interfaces, both in geophysics and beyond.

Acknowledgements

References

[1] M. Ainsworth, Dispersive and dissipative behaviour of high order discontinuous Galerkin finite element methods, Journal of Computational Physics 198 (1) (2004) 106–130, doi:10.1016/j.jcp.2004.01.004.

[2] M. Ainsworth, P. Monk, W. Muniz, Dispersive and dissipative properties of discontinuous Galerkin finite element methods for the second-order wave equation, Journal of Scientific Computing 27 (1–3) (2006) 5–40, doi:10.1007/s10915-005-9044-x.

[3] H. Bao, J. Bielak, O. Ghattas, L.F. Kallivokas, D.R. O'Hallaron, J.R. Shewchuk, J. Xu, Large-scale simulation of elastic wave propagation in heterogeneous media on parallel computers, Computer Methods in Applied Mechanics and Engineering 152 (1–2) (1998) 85–102, doi:10.1016/S0045-782(97)00183-7.

[4] D. Appelö, N.A. Petersson, A stable finite difference method for the elastic wave equation on complex geometries with free surfaces, Communications in Computational Physics 5 (1) (2009) 84–107.

[5] B. Lombard, J. Piraux, C. Gélis, J. Virieux, Free and smooth boundaries in 2-D finite-difference schemes for transient elastic waves, Geophysical Journal International 172 (2008) 252–261, doi:10.1111/j.1365-246X.2007.03620.x.

[6] B. Lombard, J. Piraux, Numerical treatment of two-dimensional interfaces for acoustic and elastic waves, Journal of Computational Physics 195 (1) (2004) 90–116, doi:10.1016/j.jcp.2003.09.024.

[7] R.W. Hoberecht, A finite volume approach to modeling injury mechanisms of blast-induced traumatic brain injury, Master's thesis, University of Washington, 2009.

[8] P. Voinovich, A. Merlen, E. Timofeev, K. Takayama, A Godunov-type finite-volume scheme for unified solid-liquid elastodynamics on arbitrary two-dimensional grids, Shock Waves 13 (3) (2003) 221–230, doi:10.1007/s00193-003-0211-4.

[9] D. Komatitsch, C. Barnes, J. Tromp, Wave propagation near a fluid-solid interface: a spectral element approach, Geophysics 65 (2) (2000) 623–631, doi:10.1190/1.1444758.

[10] E. Chaljub, Y. Capdeville, J. Vilotte, Solving elastodynamics in a fluid-solid heterogeneous sphere: a parallel spectral element approximation on non-conforming grids, Journal of Computational Physics 187 (2) (2003) 457–491, doi:10.1016/S0021-9991(03)00119-0.

[11] E. Chaljub, B. Valette, Spectral element modelling of three-dimensional wave propagation in a self-gravitating Earth with an arbitrarily stratified outer core, Geophysical Journal International 158 (1) (2004) 131–141, doi:10.1111/j.1365-246X.2004.02267.x.

[12] D. Komatitsch, S. Tsuboi, J. Tromp, The spectral-element method in seismology, in: A. Levander, G. Nolet (Eds.), Seismic Earth: Array Analysis of Broadband Seismograms, Geophysical Monograph, vol. 157, American Geophysical Union, Washington DC, USA, 2005, pp. 205–228.

[13] B. Riviere, M.F. Wheeler, A discontinuous Galerkin method applied to nonlinear parabolic equations, in: B. Cockburn, G.E. Karniadakis, C.-W. Shu (Eds.), Discontinuous Galerkin Methods. Theory, Computation and Applications, Lecture Notes in Computational Science and Engineering, vol. 11, Springer-Verlag, 2000, pp. 231–244.

[14] M.J. Grote, A. Schneebeli, D. Schötzau, Discontinuous Galerkin finite element method for the wave equation, SIAM Journal on Numerical Analysis 44 (6) (2006) 2408–2431, doi:10.1137/05063194X.

[15] E.T. Chung, B. Engquist, Optimal discontinuous Galerkin methods for wave propagation, SIAM Journal on Numerical Analysis 44 (5) (2006) 2131–2158, doi:10.1137/050641193.

[16] J.D. De Basabe, M.K. Sen, M.F. Wheeler, The interior penalty discontinuous Galerkin method for elastic wave propagation: grid dispersion, Geophysical Journal International 175 (1) (2008) 83–93, doi:10.1111/j.1365-246X.2008.03915.x.
[17] S. Delcourte, L. Fezoui, N. Glinsky-Olivier, A high-order discontinuous Galerkin method for the seismic wave propagation, in: ESAIM: Proceedings, vol. 27, 2009, pp. 70–89. doi:10.1051/proc/2009020.
[18] M. Dumbser, M. Käser, An arbitrary high-order discontinuous Galerkin method for elastic waves on unstructured meshes-II. The three-dimensional isotropic case, Geophysical Journal International 167 (1) (2006) 319, doi:10.1111/j.1365-246X.2006.03120.x.
[19] M. Käser, M. Dumbser, A highly accurate discontinuous Galerkin method for complex interfaces between solids and moving fluids, Geophysics 73 (3) (2008) T23–T35, doi:10.1190/1.2870081.
[20] J.S. Hesthaven, T. Warburton, Nodal Discontinuous Galerkin Methods: Algorithms, Analysis, and Applications, Texts in Applied Mathematics, vol. 54, Springer, 2008.
[21] R. LeVeque, Finite Volume Methods for Hyperbolic Problems, Cambridge University Press, 2002.
[22] D.A. Kopriva, Metric identities and the discontinuous spectral element method on curvilinear meshes, Journal of Scientific Computing 26 (3) (2006) 301–327, doi:10.1007/s10915-005-9070-8.
[23] D.A. Kopriva, Implementing Spectral Methods for Partial Differential Equations, Springer, 2009.
[24] M. Dumbser, M. Käser, An arbitrary high-order discontinuous Galerkin method for elastic waves on unstructured meshes-II. The three-dimensional isotropic case, Geophysical Journal International 167 (1) (2006) 319, doi:10.1111/j.1365-246X.2006.03120.x.
[25] O. Gonzalez, A.M. Stuart, A First Course in Continuum Mechanics, Cambridge Texts in Applied Mathematics, Cambridge University Press, 2008.
[26] K.-A. Feng, C.-H. Teng, M.-H. Chen, A pseudospectral penalty scheme for 2D isotropic elastic wave computations, Journal of Scientific Computing 33 (3) (2007) 313–348, doi:10.1007/s10915-007-9154-8.
[27] M. Deville, P. Fischer, E. Mund, High-Order Methods for Incompressible Fluid Flow, Cambridge Monographs on Applied and Computational Mathematics, vol. 9, Cambridge University Press, 2002.
[28] S.S. Collis, M. Heinkenschloss, Analysis of the streamline upwind/Petrov Galerkin method applied to the solution of optimal control problems, Technical Report TR02-01, Department of Computational and Applied Mathematics, Rice University, Houston, TX 77005-1892, 2002. <http://www.caam.rice.edu/heinken>.
[29] D.A. Kopriva, S.L. Woodruff, M.Y. Hussaini, Computation of electromagnetic scattering with a non-conforming discontinuous spectral element method, International Journal for Numerical Methods in Engineering 53 (1) (2002) 105–122, doi:10.1002/nme.394.
[30] D.A. Kopriva, G. Gassner, On the quadrature and weak form choices in collocation type discontinuous Galerkin spectral element methods, Journal of Scientific Computing 44 (2010) 136–155, doi:10.1007/s10915-010-9372-3.
[31] C.A. Kennedy, M.H. Carpenter, R.M. Lewis, Low-storage, explicit Runge–Kutta schemes for the compressible Navier–Stokes equations, Applied Numerical Mathematics 35 (3) (2000) 177–219, doi:10.1016/S0168-9274(99)00141-5.
[32] A.A. Kaufman, A.L. Levshin, Acoustic and Elastic Wave Fields in Geophysics, III, Methods in Geochemistry and Geophysics, vol. 39, Elsevier B.V., 2005.
[33] J.D. Achenbach, Wave Propagation in Elastic Solids, North-Holland Series in Applied Mathematics and Mechanics, vol. 16, North-Holland Publishing Company, 1973.
[34] P.C. Vinh, R.W. Ogden, On formulas for the Rayleigh wave speed, Wave Motion 39 (3) (2004) 191–197, doi:10.1016/j.wavemoti.2003.08.004.
[35] C. Burstedde, L.C. Wilcox, O. Ghattas, p4est: scalable algorithms for parallel adaptive mesh refinement on forests of octrees, SIAM Journal on Scientific Computing, submitted for publication.
[36] C. Burstedde, O. Ghattas, M. Gurnis, E. Tan, T. Tu, G. Stadler, L.C. Wilcox, S. Zhong, Scalable adaptive mantle convection simulation on petascale supercomputers, in: SC'08: Proceedings of the International Conference for High Performance Computing, Networking, Storage, and Analysis, ACM/IEEE, 2008.
[37] C. Burstedde, O. Ghattas, M. Gurnis, T. Isaac, G. Stadler, T. Warburton, L.C. Wilcox, Extreme-scale AMR, in: SC'10: Proceedings of the International Conference on High Performance Computing, Networking, Storage, and Analysis, ACM/IEEE, 2010.
[38] A.M. Dziewonski, D.L. Anderson, Preliminary reference earth model, Physics of the Earth and Planetary Interiors 25 (4) (1981) 297–356. doi:10.1016/0031-9201(81)90046-7.
[39] L. Carrington, D. Komatitsch, M. Laurenzano, M.M. Tikir, D. Michéa, N.L. Goff, A. Snavely, J. Tromp, High-frequency simulations of global seismic wave propagation using SPECFEM3D GLOBE on 62K processors, in: SC'08: Proceedings of the International Conference for High Performance Computing, Networking, Storage, and Analysis, ACM/IEEE, 2008.
[40] K. Aki, P.G. Richards, Quantitative Seismology, second ed., University Science Books, 2002.
[41] Performance applications programming interface (PAPI). <http://icl.cs.utk.edu/papi/>.